1 # Impaired immune response drives age-dependent severity of COVID-19

2 Julius Beer[1], Stefania Crotta[2], Angele Breithaupt[3], Annette Ohnemus[1], Jan Becker[1], Benedikt Sachs[1], Lisa Kern[1],

3 Miriam Llorian[4], Nadine Ebert[5, 6], Fabien Labroussaa[6, 7], Tran Thi Nhu Thao[5, 6, 8], Bettina Salome Trueeb[6, 7], Joerg

4 Jores[6, 7], Volker Thiel[5, 6, 9], Martin Beer[10], Jonas Fuchs[1], Georg Kochs[1], Andreas Wack[2], Martin Schwemmle[1, 11*],

5 Daniel Schnepf[1*]

6 [1] Institute of Virology, Medical Center University of Freiburg, Freiburg, Germany

7 [2] Immunoregulation Laboratory, The Francis Crick Institute, London, UK

8 [3] Department of Experimental Animal Facilities and Biorisk Management, Friedrich-Loeffler-Institut, Greifswald-

9 Insel Riems, Germany

10 [4] Bioinformatics and Biostatistics, The Francis Crick Institute, London, UK

11 [5] Institute of Virology and Immunology (IVI), Bern and Mittelhäusern, Switzerland

12 [6] Department of Infectious Diseases and Pathobiology, Vetsuisse Faculty, University of Bern, Bern, Switzerland

13 [7] Institute of Veterinary Bacteriology, Vetsuisse Faculty, University of Bern, Bern, Switzerland

14 [8] Graduate School for Biomedical Science, University of Bern, Bern, Switzerland

15 [9] Multidisciplinary Center for Infectious Diseases, University of Bern, Switzerland

16 [10] Institute of Diagnostic Virology, Friedrich-Loeffler-Institut, Greifswald-Insel Riems, Germany

17 [11] Faculty of Medicine, University of Freiburg, Freiburg, Germany

18 *Corresponding authors

19 # Abstract

20 SARS-CoV-2 is a highly contagious respiratory virus and the causative agent for COVID-19.

21 The severity of disease varies from mildly symptomatic to lethal and shows an extraordinary

22 correlation with increasing age, which represents the major risk factor for severe COVID-19[1].

23 However, the precise pathomechanisms leading to aggravated disease in the elderly are

24 currently unknown. Delayed and insufficient antiviral immune responses early after infection

25 as well as dysregulated and overshooting immunopathological processes late during disease

26 were suggested as possible mechanisms. Here we show that the age-dependent increase of

27 COVID-19 severity is caused by the disruption of a timely and well-coordinated innate and

28 adaptive immune response due to impaired interferon (IFN) responses. To overcome the

29 limitations of mechanistic studies in humans, we generated a mouse model for severe

30 COVID-19 and compared the kinetics of the immune responses in adult and aged mice at

31 different time points after infection. Aggravated disease in aged mice was characterized by a

32 diminished IFN-γ response and excessive virus replication. Accordingly, adult IFN-γ receptor-

33 deficient mice phenocopied the age-related disease severity and supplementation of IFN-γ

34 reversed the increased disease susceptibility of aged mice.

35 Mimicking impaired type I IFN immunity in adult and aged mice, a second major risk factor

36 for severe COVID-19[2-4], we found that therapeutic treatment with IFN-λ in adult and a

37 combinatorial treatment with IFN-γ and IFN-λ in aged $Ifnar1^{-/-}$ mice was highly efficient in

38 protecting against severe disease.

39 Our findings provide an explanation for the age-dependent disease severity of COVID-19 and

40 clarify the nonredundant antiviral functions of type I, II and III IFNs during SARS-CoV-2

41 infection in an age-dependent manner. Based on our data, we suggest that highly vulnerable

42 individuals combining both risk factors, advanced age and an impaired type I IFN immunity,

43 may greatly benefit from immunotherapy combining IFN-γ and IFN-λ.

Introduction

Within two years since its introduction into the human population, SARS-CoV-2 has caused more than 450 million confirmed cases of COVID-19 leading to about 6 million deaths globally as of March 2022 [*WHO coronavirus dashboard*]. Interestingly, the burden of severe disease and mortality is not equally distributed across age groups and shows an extraordinary log-linear correlation with increasing age for individuals older than 30 years[1]. To enable the rational design of effective therapeutics and prevention strategies for vulnerable groups, a better understanding of disease-causing mechanisms is urgently needed.

One common hallmark of severe COVID-19 and advanced age is a diminished and delayed innate immune response affecting the timely production of interferons (IFNs)[5-8]. Type I, II and III IFNs, also called IFN-α/β, IFN-γ and IFN-λ, respectively, are known antiviral cytokines which are rapidly produced by the host upon recognition of viral material. IFNs orchestrate an immediate cell intrinsic innate immune response by upregulating expression levels of interferon-stimulated genes (ISGs) and initiate the subsequent adaptive immune response by the recruitment and activation of immune cells[9-12]. The delayed and diminished IFN response in severe COVID-19 is associated with a late and dysregulated inflammatory gene expression signature[8,12-14], likely due to enhanced tissue damage caused by an insufficient control of virus replication. The clinical relevance of a well-functioning IFN response was emphasized by the finding that 3.5 % of patients with life-threatening COVID-19 had genetic defects in genes involved in virus recognition, IFN production and signaling, including *TLR3*, *TBK1*, *IRF3*, *IRF7*, *IFNAR1* and *IFNAR2*[2]. In addition, type I IFN neutralizing antibodies were detected in another 10 % of critically ill COVID-19 patients with a tendency of increased frequency in the elderly[4]. Even though clinical penetrance of neutralizing antibodies against type I IFNs for severe COVID-19 is not complete[15], they may promote lethal disease progression in up to 20 % of deaths caused by SARS-CoV-2 infection[3]. The markedly lower risk of children to develop severe COVID-19 on the other hand correlates with an increased basal expression level of the pattern-recognition receptors (PRRs) MDA5 and RIG-I leading to a stronger innate antiviral immune response upon SARS-CoV-2 infection compared with adults[16,17]. In agreement, an early type I IFN response in immune cells was associated with the containment of virus dissemination preventing viral pneumonia[18]. However, despite its important endogenous role, type I IFNs have limited therapeutic potential due to their ability to augment disease late during infection[19].

In contrast, type III IFNs lack such inflammatory effects[20,21] and can be used as potent antiviral treatments, even in the absence of a fully functional type I IFN immunity[22,23]. A higher IFN-λ to IFN-α/β ratio in critically ill COVID-19 patients correlated with an improved disease outcome, and patients with high expression levels of IFN-λ showed decreased viral loads and an accelerated viral clearance[13]. In line, a small phase II placebo-controlled randomized trial in humans found that treatment of SARS-CoV-2 infected patients with IFN-λ could accelerate viral decline and clearance[24].

84   The role of type II IFN during COVID-19 on the other hand is much less clear. Whereas one
85   study reported that the epithelial response to IFN-γ would promote SARS-CoV-2 infection[25],
86   another one demonstrated significant inhibition of virus replication[26]. NK cells from
87   ambulant COVID-19 patients showed increased production of IFN-γ, whereas NK cells from
88   patients with severe COVID-19 produced only low levels of IFN-γ and TNF[27]. This study
89   further demonstrated that an untimely TGF-β response, a cytokine suppressing IFN-γ
90   mediated functions, was limiting the antiviral activity of NK cells. In agreement, others found
91   that NK cells from severe COVID-19 patients were dysfunctional showing an impairment of
92   antiviral activity that was associated with a diminished production of IFN-γ and TNF[28].

93   Despite the vast amount of clinical data available by now, many questions regarding the
94   disease-causing mechanisms in the elderly remain unresolved. Small animal models are
95   essential to overcome the limitations of human sample heterogeneity and availability.
96   However, most clinical isolates of SARS-CoV-2 cannot infect standard inbred mice, with few
97   exceptions only causing asymptomatic infection[29,30]. Whereas knock-in mice expressing
98   human angiotensin I-converting enzyme 2 (*ACE2*), the receptor for SARS-CoV-2, are
99   permissive for infection with clinical isolates, they do not develop severe or lethal disease[31-
100   33]. Another widely used model that does support severe to lethal disease upon SARS-CoV-2
101   infection are transgenic mice expressing *ACE2* under the cytokeratin-18 (K18) promotor.
102   While this mouse strain is suitable to test various intervention strategies[34,35], its use to study
103   mechanisms of disease is limited, e.g. by artifactual neuroinvasion of the virus due to
104   abundant and non-physiological expression of the viral receptor[36]. To be able to use existing
105   standard inbred mouse strains, including knockout mice, researchers developed mouse-
106   adapted SARS-CoV-2 strains either by *in silico* design followed by reverse genetics[37], by serial
107   passaging[38-42] or by a combination of both[43].

108   In this study, we describe the generation of a highly pathogenic mouse-adapted SARS-CoV-2
109   strain (designated SARS-CoV-2 MA20) that dose-dependently causes mild, severe or even
110   lethal disease progression in 8-20-week-old adult C57BL/6 wild type mice. In 36-60-week-old
111   aged C57BL/6 mice, disease severity was strongly enhanced and correlated with (i) the lack
112   of an early and well-coordinated innate and adaptive immune response, (ii) a markedly
113   increased viral load, and (iii) a late inflammatory response. Direct comparison of adult and
114   aged knockout mice showed that defective type I and type II IFN signaling phenocopies
115   enhanced disease progression in aged mice, providing a mechanistic explanation for the age-
116   related increase in disease susceptibility during SARS-CoV-2 infection.

117   Using adult mice lacking a functional IFN-α/β receptor (*Ifnar1*^{-/-}) to mimic an impaired type I
118   IFN immunity[2-4], we show that prophylactic or therapeutic administration of IFN-λ efficiently
119   protected such lethally infected mice. Nevertheless, IFN-λ treatment alone had limited
120   protective effects in highly vulnerable aged *Ifnar1*^{-/-} mice. However, administration of IFN-γ
121   in aged wild type mice reversed the age-dependent enhanced disease phenotype, and a
122   combinatorial treatment with IFN-λ and IFN-γ even protected highly vulnerable aged *Ifnar1*^{-/-}
123   mice against lethal disease.

124   By generating and employing a mouse model for severe COVID-19 we identified an age-
125   dependent impairment of type I and type II IFN responses as a critical pathomechanism that

126 drives the virulence of SARS-CoV-2 in aged hosts. This novel insight was successfully
127 translated into an immunomodulatory treatment strategy that prevented SARS-CoV-2-
128 induced lethality in a highly susceptible disease model that mimics impaired type I IFN
129 immunity and advanced age.

Results

**Type I and type III IFNs synergize to limit SARS-CoV-2 replication and protect aged mice
against symptomatic disease**

133 To dissect the individual and combinatorial role of type I and type III IFNs in limiting SARS-
134 CoV-2 replication, we compared the replication kinetics of a mouse-adapted but largely non-
135 virulent SARS-CoV-2 strain (SARS-CoV-2 MA[37]) in IFN receptor-deficient and C57BL/6 wild
136 type (WT) mice. Three days post infection (d p. i.) we found about 10-fold increased viral
137 loads in lungs and upper airways of mice lacking functional type I (*Ifnar1*$^{-/-}$) or type III IFN
138 receptors (*Ifnlr1*$^{-/-}$) (**Figure 1A** and **Figure S1A**). By day 5 p. i. most WT mice had cleared the
139 virus, whereas *Ifnar1*$^{-/-}$ and especially *Ifnlr1*$^{-/-}$ mice continued to have high viral titers in their
140 lungs (**Figure 1A**). Conversely, prophylactic or therapeutic administration of either IFN-$\alpha_{B/D}$[22]
141 to *Ifnlr1*$^{-/-}$ or IFN-λ1/3[44] to *Ifnar1*$^{-/-}$ mice reduced lung viral loads on day 3 p. i. by several
142 orders of magnitude (**Figure 1B** and **Figure S1B**). Combinatorial loss of type I and type III IFN
143 signaling in *Ifnar1*$^{-/-}$*Ifnlr1*$^{-/-}$ mice led to excessive replication and prolonged persistence of the
144 virus in upper airways and lungs (**Figure 1A** and **Figure S1A**). Immunohistochemical analyses
145 confirmed increased virus replication and prolonged virus persistence in *Ifnar1*$^{-/-}$*Ifnlr1*$^{-/-}$
146 compared with WT mice (**Figure S1C-D**), mainly affecting the bronchial epithelium and only
147 scarcely alveolar epithelial cells. Lung tissue damage (**Figure S1E**) and necrotizing bronchitis
148 (**Figure S1F**) followed the pattern of increased and prolonged virus replication in *Ifnar1*$^{-/-}$
149 *Ifnlr1*$^{-/-}$ mice. However, despite increased and prolonged viral replication and tissue damage,
150 we did not observe weight loss or other signs of disease in adult mice lacking type I and/or
151 type III IFN responses (**Figure 1C**). In contrast, using aged animals in an identical infection
152 setting, we observed significantly increased weight loss in *Ifnar1*$^{-/-}$, *Ifnlr1*$^{-/-}$ and *Ifnar1*$^{-/-}$*Ifnlr1*$^{-/-}$
153 $^{-/-}$ mice compared with age-matched WT controls (**Figure 1D**), sporadically even leading to
154 lethal disease progression in case of *Ifnar1*$^{-/-}$*Ifnlr1*$^{-/-}$ mice (**Figure S1G**). Of note, we did not
155 observe increased weight loss in aged WT mice compared with adult controls (**Figure 1C and
156 D**), indicating that a combination of advanced age and impaired type I/III IFN immunity is
157 required to result in symptomatic disease during infection with the SARS-CoV-2 MA strain.
158 Taken together these data demonstrated that type I and type III IFNs synergize to limit
159 excessive SARS-CoV-2 replication, to expedite virus clearance and to protect against
160 symptomatic disease in aged mice.

Advanced age correlates with increased viral loads and diminished immune responses

To gain more insights into the age-dependent disease phenotype of SARS-CoV-2 MA, we compared tissue sections from upper airway and lung samples of infected adult and aged *Ifnar1*$^{-/-}$ mice. Three days p. i., we detected increased antigen load in upper airways and lungs as well as enhanced bronchial necrosis in aged *Ifnar1*$^{-/-}$ mice (**Figure S1H-J**)*.* Comparing viral growth kinetics in adult and aged WT, *Ifnar1*$^{-/-}$, *Ifnlr1*$^{-/-}$, and *Ifnar1*$^{-/-}$*Ifnlr1*$^{-/-}$ mice, we confirmed the age-dependent increase in virus replication at 3 d p. i., irrespectively of genotype (**Figure 1E-F** and **Figure S1K**). To identify impaired antiviral or enhanced pro-viral pathways facilitating virus replication in aged mice that are independent of type I/III IFN signaling, we performed transcriptome analyses using lung samples of infected or mock-treated adult and aged *Ifnar1*$^{-/-}$ mice. Gene Set Enrichment Analyses (GSEA) comparing mock-treated (**Figure 1G**) or infected (**Figure 1H**) adult and aged *Ifnar1*$^{-/-}$ mice both identified an age-related increase in pathways involved in the function of ciliated cells, possibly suggesting age-dependent differences in the cellular composition of the lung. Whereas no pathways were significantly enriched in uninfected adults compared to aged mice, lung tissue samples from infected adult mice showed a significant enrichment in pathways involved in the production and response to IFN-γ, NK cell-mediated immunity, immune cell activation and adaptive immune responses (**Figure 1H**) which indicated a versatile and robust immune response in adult animals. The disruption of a timely and well-coordinated innate and adaptive immune response in aged mice upon SARS-CoV-2 infection could well explain impaired virus control, ultimately leading to enhanced disease progression.

These data demonstrate that the age-dependent increase in virus replication is independent of type I and type III IFN signaling, but correlates with an age-related impaired immune response affecting IFN-γ production, NK cell mediated immunity and general immune cell activation.

Rapid host adaptation by serial passaging in type I/III IFN receptor-deficient C57BL/6 mice

To study the age-related pathophysiology of SARS-CoV-2-induced disease in more detail and to test possible intervention strategies, we generated a mouse model resembling severe COVID-19 by serially passaging the SARS-CoV-2 MA strain *in vivo*. In total, we performed four independent passaging series, two in C57BL/6 WT (WT A and B) and two in *Ifnar1*$^{-/-}$*Ifnlr1*$^{-/-}$ mice (DKO A and B) (**Figure 2A**). From passage 10 onwards, *Ifnar1*$^{-/-}$*Ifnlr1*$^{-/-}$ but not WT mice were losing increasing amounts of their initial body weight (**Figure 2B**). Whereas viral titers in lungs remained relatively stable until passage 20, viral loads in the upper airways increased from passage 14 onwards for series WT B, DKO A and DKO B (**Figure S2A-B**). To identify which passaging series contained pathogenic variants, we infected groups of C57BL/6 WT mice with passage 20 (P20) lung homogenates containing 10^4 plaque forming units (PFU) of virus and followed the course of disease and survival rates (**Figure 2C**). Virus variants derived from passaging series WT A and B did not induce severe signs of disease, whereas P20 homogenates from passaging series DKO A and DKO B induced severe weight loss and even 40 % lethality in adult C57BL/6 WT mice in case of DKO A P20. Using plaque-

201 purified (PP) virus stocks derived from DKO A and DKO B P20 lung homogenates, we
202 confirmed the successful generation of a pathogenic mouse-adapted SARS-CoV-2 variant
203 that emerged in passaging series DKO A (**Figure S2C**). Virus genome sequencing revealed
204 that this variant, named SARS-CoV-2 MA20 (MA20), acquired eight additional amino acid
205 changes compared with the parental SARS-CoV-2 MA strain (**Figure 2D**), three in S (T250A,
206 K417N and Q493H), one in M (T7I) and four in ORF1ab (A1997V, T3058I, D4165Y and
207 T4174A) that translate into A1179V in nsp3, T295I in nsp4, and D25Y and T34A in nsp9. Of
208 note, identical or similar amino acid substitutions such as the Q493H and K417N in the spike
209 protein are also present in other mouse-adapted SARS-CoV-2 variants[39,40,43] or circulating
210 variants of concern (VOCs) including B.1.1.529 (Omicron) (**Figure S2D-E**). Despite its
211 increased pathogenicity in mice, SARS-CoV-2 MA20 replication was strongly attenuated in
212 human Calu-3 and simian Vero E6 cells (**Figure 2E** and **Figure S2F**). In addition, MA20 is even
213 better neutralized by sera from vaccinated humans compared with the B.1.617.2 (Delta)
214 variant (**Figure S2G**). Using doses from 10^2-10^4 PFU MA20, we could model mild, moderate,
215 or even lethal SARS-CoV-2-induced disease progression in adult C57BL/6 WT mice (**Figure
216 2F**). By infecting age- and sex-matched C57BL/6, BALB/c and 129/sv mice with 10^3 PFU
217 MA20, we found that BALB/c mice were highly susceptible with a survival rate of only 30 %,
218 that 129/sv mice were mostly resistant to disease, and that C57BL/6 showed intermediate
219 susceptibility with substantial weight loss but a survival rate of 90 % (**Figure 2G**).
220 Next, we performed virus growth kinetics in groups of C57BL/6 WT mice using 10^3 PFU of
221 MA20 and monitored virus shedding via the nostrils (**Figure 3A**) and virus replication in
222 upper airways (**Figure 3B**) and lungs (**Figure 3C**). Infection-induced gene expression levels of
223 inflammatory cytokines such as *Il6* and *Tnf*, type I (*Ifna4* and *Ifnb*) and type III IFNs (*Ifnl2/3*)
224 as well as IFN-stimulated genes (ISGs) such as *Mx1*, *Isg15* and *Stat1* peaked simultaneously
225 with peak viral loads on day two p. i. in lungs and upper airways (**Figure 3D and Figure S2H**).
226 By day seven p. i., no infectious virus could be detected anymore which was in line with
227 histopathological findings that viral antigens were mostly cleared by day 7 (**Figure 3E-F**).
228 Despite rapidly decreasing lung viral loads (**Figure 3C**), lung tissue damage remained at high
229 scores until day 7 (**Figure 3G**). Compared with the less virulent SARS-CoV-2 MA strain, the
230 highly pathogenic SARS-CoV-2 MA20 variant caused a more widespread infection of the lung
231 tissue as indicated by increased antigen-positive areas (**Figure S1I and 3F**; about 10 % mean
232 antigen detection in SARS-CoV-2 MA infected adult *Ifnar1*$^{-/-}$ 3 d p. i., compared with about 67
233 % mean antigen detection in SARS-CoV-2 MA20 infected adult WT mice 3 d p. i.). Besides the
234 bronchial epithelium, mainly alveolar epithelial cells were found to be virus-positive, in
235 particular type 2 pneumocytes. In line with an acute viral pneumonia, lung lesions were
236 characterized by necrotizing bronchitis, most severely affecting mice on day 3 p. i. (**Figure
237 3H**). The extent and severity decreased over time, but bronchial lesions were still detectable
238 until day 7 p. i. in all animals analyzed. Perivascular infiltrates comprised mainly of
239 neutrophils and few lymphocytes. Focal to multifocal necrosis of the alveolar epithelium was
240 associated with minimal to moderate alveolar infiltrates. Tissue regeneration in some
241 animals could be detected as early as 3 d p. i. and consistently increased until day 7 p. i.
242 (**Figure 3I**), as indicated by bronchial epithelial hypertrophy and hyperplasia as well as type 2

243 pneumocyte hyperplasia. In single cases, we found atypical multinucleated (syncytial) cells,
244 increased mucus production and endotheliitis. Numerous examples for leukocyte rolling
245 were found in blood vessels of infected animals, indicating endothelial and/or immune cell
246 activation. Interstitial infiltrates were rarely detected. Neither vasculitis nor diffuse alveolar
247 damage was detected. Examining other organs by RT-qPCR for the presence of viral RNA, we
248 found low levels in brain and spleen samples and infrequently positive heart, liver, intestine
249 and kidney samples, indicating that replication of SARS-CoV-2 MA20 is mainly restricted to
250 the upper and lower respiratory tract in adult mice (**Figure 3J**).
251 These data show that serial passaging in *Ifnar1*^{-/-}*Ifnlr1*^{-/-} mice facilitated rapid host adaption,
252 which resulted in the highly virulent SARS-CoV-2 MA20 variant that can be used to model
253 mild, severe or even lethal COVID-19 in standard inbred mice.

Enhanced disease progression in aged mice correlates with a diminished immune response leading to insufficient control of virus replication

256 Disease severity and risk of death due to COVID-19 shows a log-linear correlation with
257 advanced age in humans[1]. Correspondingly, aged mice showed a massively enhanced
258 disease phenotype and increased lethality upon infection with MA20 compared with adult
259 counterparts (**Figure S3A**). To mechanistically address the age-dependent enhanced disease
260 progression, we chose infection conditions which cause a comparable weight loss from
261 which adult but not aged mice could recover (**Figure 4A**) and measured virus replication
262 kinetics, determined systemic dissemination of viral material, assessed lung tissue damage
263 and compared kinetics of the age-dependent immune response profiles in infected lungs.
264 Between day 3 and 5 p. i., virus replication in upper airways (**Figure 4B**) and lungs (**Figure 4C**)
265 of aged mice was found to be increased by one to two orders of magnitude compared with
266 genetically identical adult controls, demonstrating an age-dependent impairment of virus
267 control. Immunohistochemistry of infected lung sections confirmed significantly increased
268 antigen scores in aged mice compared with adult counterparts (**Figure 4D-E**). For both, adult
269 and aged mice, viral antigen was found abundantly in the bronchial and alveolar epithelium,
270 in particular in type 2 pneumocytes. Intriguingly, histopathological analyses revealed that
271 overall lung lesion scores were comparable between both age groups (**Figure 4F**), even
272 though signs of disease were much more pronounced in MA20-infected aged mice. Acute
273 necrotizing bronchitis showed only a slight tendency to be increased in aged mice (**Figure
274 4G**), and tissue regeneration indicated by bronchial epithelial hypertrophy and hyperplasia
275 as well as type 2 pneumocyte hyperplasia appeared to be less prominent in aged animals
276 (**Figure 4H**). Investigating the potential systemic dissemination of virus material, we found
277 viral RNA levels to be significantly increased in heart, liver, kidney and brain samples of aged
278 mice compared with adult controls on day 4 and 5 p. i. (**Figure 4I**). However, using
279 immunohistochemistry and RNA in situ hybridization methods, no viral antigen or RNA could
280 be detected in heart and brain samples (data not shown). Furthermore, histology of the
281 brain and heart revealed no abnormalities and neither immunohistochemistry for T-cells
282 (CD3) nor microglia/macrophages (Iba-1) identified inflammatory infiltrates or microglial
283 reaction (data not shown).

284   Next, we compared the kinetics of transcriptional responses in MA20-infected lungs of adult
285   and aged mice. Principal component analysis of the lung transcriptome showed that
286   uninfected adult and aged mice closely clustered together, indicating that basal gene
287   expression profiles in uninfected lungs of adult and aged mice were rather similar (**Figure
288   5A**). In contrast, transcriptional profiles of infected lung samples clearly diverged dependent
289   on the respective age group for all time points p. i. analyzed, demonstrating a drastically
290   different transcriptional response to SARS-CoV-2 infection between the two age groups
291   (**Figure 5A**). Gene Set Enrichment Analyses (GSEA) comparing each time point p. i. between
292   adult and aged mice revealed that adult animals mounted a rapid and versatile innate and
293   adaptive immune response. In contrast, the immune response of aged animals was delayed,
294   reduced in pathways leading to adaptive immunity, and mainly pro-inflammatory. From 3 d
295   p. i. onwards, innate immune pathways involving IFN-γ signaling and NK cell activity but also
296   adaptive cellular and humoral immune responses were significantly enriched in adult
297   animals compared with aged controls (**Figure 5B**). By contrast, in aged animals primarily pro-
298   inflammatory pathways driven by IL-6, IL-1 and type I IFN were found to be significantly
299   enriched upon day 4 p. i. compared with samples derived from adult animals. Pairwise
300   comparison of infected to mock lung samples from adult or aged animals at different time
301   points post infection using the Ingenuity Pathway Analysis (IPA) confirmed that adult animals
302   were mounting a rapid and well-orchestrated innate and adaptive immune response,
303   characterized by the initiation of PRR signaling, NK cell activation, and the production and
304   response to Th1/Th2 cytokines (**Figure 5C**). In contrast, aged animals showed a reduced,
305   delayed and more pro-inflammatory response. In addition to IL-6- and IL-1-driven pathways,
306   IPA also identified active processes of pulmonary fibrosis and hypoxia-induced gene
307   regulation in infected lung tissue of aged mice (**Figure 5C**). Intriguingly, aged animals also
308   showed an early and strong IL-10 response[45,46] which further emphasizes the imbalanced
309   early immune response in aged animals and might explain the lack of a potent immune
310   response initiated by IFN-γ and other immune activating cytokines as observed in adult mice.
311   Taken together these data demonstrate that the age-dependent increase in disease
312   susceptibility upon SARS-CoV-2 infection correlates with an impaired virus control due to
313   imbalanced and insufficient innate and adaptive immune responses.

**Combinatorial defects in type I and type II IFN signaling phenocopies age-dependent
disease susceptibility**

316   Using 300 PFU of the highly virulent MA20 strain we determined the disease susceptibility of
317   adult mice lacking functional type I and/or type III IFN systems. Single knockout mice
318   deficient in type I or type III IFN-mediated responses had comparable survival rates as WT
319   mice but suffered from increased and prolonged weight loss. In contrast, mice lacking both
320   systems rapidly lost weight, and most animals reached experimental endpoints and had to
321   be euthanized (**Figure 6A**). As the disease course of adult *Ifnar1$^{-/-}$Ifnlr1$^{-/-}$* mice closely
322   resembled the one in aged WT mice (**Figure 4A**), we performed low-dose infection
323   experiments with MA20 in adult and aged mice of matching genotypes to assess whether
324   the age-dependent increase in disease susceptibility was caused by an impaired IFN

325   response. Using 30 PFU of MA20, we detected a significantly enhanced disease progression
326   in aged WT, and in addition significantly increased lethality in aged *Ifnar1*^{-/-}, *Ifnlr1*^{-/-} and
327   *Ifnar1*^{-/-}*Ifnlr1*^{-/-} mice compared with their respective adult controls (**Figure 6B-E**). These
328   results indicated that individual or combinatorial loss of type I and type III IFN signaling does
329   not recapitulate the mechanisms underlying increased disease severity in aged mice.
330   Because GSEA and IPA of SARS-CoV-2 infected lung samples both identified an age-
331   dependent reduction in the IFN-γ-mediated immune response to infection, we also assessed
332   the contribution of an impaired type II IFN response to the age-related phenotype.
333   Interestingly, a marked weight loss within 4 d p. i. was only observed in aged but not adult
334   WT, *Ifnar1*^{-/-}, *Ifnlr1*^{-/-} and *Ifnar1*^{-/-}*Ifnlr1*^{-/-} mice (**Figure 6B-E**), whereas weight loss of adult
335   *Ifngr1*^{-/-} mice within the first 4 days of infection was comparable to that of aged *Ifngr1*^{-/-} mice
336   (**Figure 6F**). This supports our previous findings obtained by transcriptional profiling (**Figure**
337   **1H and 5B-C**) that suggested a relevant contribution of an early and potent IFN-γ response to
338   prevent SARS-CoV-2-induced disease in adult mice. Further supporting this hypothesis, initial
339   weight loss and survival rates of infected adult and aged *Ifnar1*^{-/-}*Ifngr1*^{-/-} were found to be
340   nearly identical (**Figure 6G**). In addition, adult *Stat1*-deficient mice lacking the ability to
341   respond to any type of IFN, were equally susceptible to SARS-CoV-2-induced disease and
342   lethality as their aged counterparts (**Figure 6H**).
343   Collectively, these data suggested that excessive virus replication promoted by an impaired
344   type I IFN system in combination with impaired IFN-γ-mediated immune responses can
345   account for the observed high SARS-CoV-2 disease susceptibility of aged mice.

346   **Therapeutic administration of IFN-λ prevents SARS-CoV-2-induced lethality and**
347   **supplementation of IFN-γ reverses the age-dependent disease phenotype**

348   Experiments using *Ifnar1*^{-/-} and *Ifnar1*^{-/-}*Ifnlr1*^{-/-} mice demonstrated that endogenously
349   produced type III IFNs can partially substitute for a dysfunctional type I IFN immunity[2-4],
350   thereby protecting against lethal disease progression (**Figure 6A**). Therefore, we evaluated
351   the antiviral potential of IFN-λ as a drug candidate[47] in the context of a dysfunctional type I
352   IFN immunity. We could demonstrate that a single prophylactic administration of 2 μg IFN-
353   λ1/3[44] one day prior to infection or a therapeutic regimen of 3 μg/d for one week starting
354   one day after infection, efficiently prevented lethal disease progression in adult *Ifnar1*^{-/-} mice
355   (**Figure 7A**). However, modeling advanced age in combination with dysfunctional type I IFN
356   immunity by using aged *Ifnar1*^{-/-} mice, we found that a single prophylactic administration of
357   IFN-λ was insufficient to significantly reduce disease burden in such highly susceptible mice
358   (**Figure 7B**), whereas therapeutic administration of IFN-λ showed some residual protective
359   activity by significantly reducing weight loss with a trend towards increased survival rates
360   (**Figure 7B**). Of note, therapeutic application of IFN-λ efficiently protected aged WT animals
361   with functional type I IFN immunity against SARS-CoV-2 induced disease and lethality (**Figure**
362   **S3B**). Next, we treated aged WT mice daily with 2 μg IFN-γ from -1 to 7 d p. i. to test whether
363   supplementation of IFN-γ could reverse the age-dependent enhanced disease severity upon
364   SARS-CoV-2 infection. Infection with 200 PFU MA20 caused substantial weight loss and lethal
365   disease progression in 5 out of 8 aged WT mice, whereas aged WT mice supplemented with

366 IFN-γ showed a significantly reduced weight loss and an increased survival rate which was
367 nearly identical with the disease course of adult WT mice (**Figure 7C**). Encouraged by the
368 positive results of IFN-λ in adult *Ifnar1$^{-/-}$* and those of IFN-γ in aged WT animals, we next
369 tested a combination of both treatments in an attempt to protect highly susceptible aged
370 mice with a defective type I IFN system. Whereas individual therapeutic treatment regimens
371 with either IFN-λ or IFN-γ in aged *Ifnar1$^{-/-}$* both conferred only limited protection against
372 SARS-CoV-2 induced disease and lethality (**Figure 7B and S3C**), the combinatorial therapeutic
373 treatment with IFN-λ1/3 and IFN-γ prevented morbidity exceeding 10 % of body weight loss
374 in an otherwise lethal infection (**Figure 7D**).

375 Taken together these data demonstrated that (i) the drug candidate IFN-λ1/3 could
376 efficiently prevent lethal disease progression in adult mice with defective type I IFN
377 immunity, that (ii) supplementation of IFN-γ could reverse the age-dependent enhanced
378 disease progression and that (iii) the combination of both treatments rescued lethally
379 infected aged mice lacking type I IFN responses (**Figure S4**).

Discussion

381 Two major risk factors for severe COVID-19 are advanced age[1] and an impaired IFN-
382 mediated immunity[2-4]. For the rational design of effective therapeutics and prevention
383 strategies targeting the respective risk groups, a better understanding of the disease-causing
384 mechanisms is urgently needed. Small animal models faithfully recapitulating characteristics
385 of human disease are pivotal to overcome these limitations. In this study, we generated a
386 highly pathogenic mouse-adapted SARS-CoV-2 variant that can be used to model mild,
387 moderate or severe COVID-19 as well as the age-associated aggravation of disease in
388 standard inbred mice.

389 Using this small animal model, we found that the age-dependent increase in disease severity
390 is driven by an impaired interferon response which causes a delayed, insufficient and
391 dysregulated innate and adaptive immune response in the aged host. Transcriptome
392 analyses of infected lungs from mature adult and middle-aged C57BL/6 mice revealed that
393 adult mice initiated a rapid and well-coordinated innate and adaptive immune response,
394 which was associated with high IFN-γ and low IL-10 expression levels. This effective and
395 timely immune response in adults limited viral loads, mediated rapid viral clearance, and
396 efficiently prevented the development of severe disease. In aged mice, by contrast, virus
397 replication was markedly increased which correlated with the absence of effective antiviral
398 immune responses. Instead, aged mice showed strong IL-6- and IL-1-mediated responses
399 associated with low IFN-γ and high IL-10 expression levels. The markedly different IFN-γ to
400 IL-10 ratio likely explains the effective immune response, including NK cell mediated
401 immunity, efficient antigen presentation, lymphocyte activation, and immunoglobulin
402 production in adult mice that leads to the favorable disease outcome compared with aged
403 counterparts (**Figure S4**).

404 Interestingly, in spite of the strongly increased viral loads and the enhanced disease
405 progression in aged animals, lung tissue damage was comparable between both age groups.
406 This finding possibly indicates a functional impairment of the infected aged lung rather than

407   excessive cellular damage that would be detected using classical histological methods such
408   as H&E stainings. Alternatively, it is possible that aged mice suffered from a systemic
409   manifestation of disease due to overshooting cytokine production[48] or virus dissemination to
410   other organs. Indeed, RT-qPCR analyses revealed elevated viral RNA levels in both heart and
411   brain samples of aged mice. However, neither signs of inflammation or immune cell
412   infiltrations were detected nor were viral RNA-positive cells found in heart and brain
413   samples from aged mice using highly sensitive RNA in situ hybridization methods, arguing
414   against a systemic dissemination of the virus in aged animals.

415   To test whether an impaired IFN response would indeed phenocopy the enhanced disease
416   progression in the aged host, we directly compared adult and aged mice with individual or
417   combinatorial deficiencies in the various IFN pathways. We found that type I and type III IFNs
418   limited disease susceptibility and lethality but genetic defects in these pathways did not
419   faithfully recapitulate the age-dependent enhanced disease phenotype. Importantly,
420   however, adult *Ifngr1*^{-/-} mice with a deficient type II IFN system suffered from increased
421   disease severity that closely resembled the disease course of aged wild type mice.
422   Nevertheless, aged *Ifngr1*^{-/-} mice still showed enhanced disease progression and increased
423   lethality compared with their younger counterparts, indicating that additional mechanisms
424   are promoting the age-dependent disease severity. Indeed, adult *Ifnar1*^{-/-}*Ifngr1*^{-/-} mice
425   lacking functional type I and type II IFN signaling, showed the same degree of severe weight
426   loss and poor survival rates as their aged counterparts, demonstrating a defining role of
427   diminished type I and type II IFN responses driving the age-dependent virulence of SARS-
428   CoV-2.

429   We therefore hypothesize that the age-dependent impairment of IFN-γ-mediated responses
430   causes the impaired NK cell activation, reduced antigen presentation and diminished
431   lymphocyte activation that we see in our transcriptome data, whereas the impaired type I
432   IFN immunity facilitates virus replication due to reduced cell-intrinsic antiviral immunity. In
433   agreement with our finding that adult *Ifngr1*^{-/-} mice phenocopied the disease course of aged
434   wild type animals, we found that treatment of aged mice with IFN-γ prevented severe
435   disease progression, supporting the view that IFN-γ limits age-dependent COVID-19 severity.
436   By comparing children and adults, other researchers found that increased expression levels
437   of PRRs such as MDA5 and RIG-I maintain a tonic IFN-activated antiviral state in the airways
438   which appears to contribute to the high resistance of young individuals against severe
439   COVID-19[16,17]. However, it is unclear whether such mechanisms, which may explain the
440   elevated baseline of type I and type III IFNs, would affect IFN-γ production. Whereas type I
441   and type III IFNs are produced mainly by dendritic cells as well as infected epithelial cells
442   upon activation of PRRs[11], IFN-γ is mainly produced by NK and T cells and involves distinct
443   transcription factors such as Eomes and T-bet in its regulation[49]. Of note, adult mice in our
444   study showed significantly increased expression levels of T-bet in their infected lungs
445   compared with aged mice.

446   Additional studies are required to determine which pathways and cell types are involved in
447   the detection of SARS-CoV-2 infection, and which cells produce the respective types of
448   interferon to prevent severe disease. The identification of cell types that fail to produce IFN-

γ and/or fail to adequately respond to this cytokine in the aged organism may enable the development of novel strategies that aim at preventing or reversing such pathological processes. A recent study showed that soluble factors in plasma from severe COVID-19 patients reversibly interfered with the antiviral activity of NK cells and their capacity to mount an appropriate IFN-γ and TNF response that otherwise was associated with a favorable disease outcome[28]. Interestingly, others suggested a potential disease-driving role of IFN-γ in combination with TNF, possibly inducing inflammatory cell death during severe COVID-19 via PANoptosis[50]. However, we observed that the protective effects of endogenous or exogenous IFN-γ during SARS-CoV-2 infection clearly outweigh possible detrimental effects in our infection model. Similarly, two recent studies raised awareness that continuous IFN-λ signaling could hamper with efficient lung repair after viral infection[51,52]. However, in our COVID-19 mouse model, IFN-λ deficiency led to increased and prolonged viral replication causing enhanced disease and delayed recovery. Vice versa, both prophylactic and therapeutic treatment with IFN-λ strongly reduced viral loads in the lung and efficiently prevented disease deterioration in lethally infected aged mice or adult animals lacking type I IFN immunity. This strongly indicates that the protective effects of IFN-λ during severe SARS-CoV-2 infections outcompete potential adverse effects. Notably, individual therapeutic treatment of infected aged *Ifnar1*$^{-/-}$ mice, a model combining two of the most detrimental risk factors for severe COVID-19 in humans[1,3], with either IFN-γ or IFN-λ had limited success in preventing severe disease and lethality. However, the combination of both cytokines proved to be highly efficient. We therefore hypothesize that exogenous IFN-γ rescues the age-related impairment of cellular immune responses, whereas IFN-λ compensates for the compromised cell-intrinsic antiviral immunity in epithelial cells. Both cytokines may also improve DC migration into draining lymph nodes facilitating T cell activation[53], a process which is impaired in infected aged mice due to elevated levels of prostaglandin D_2 and its upstream phospholipase PLA2G2D[8,54-56]. Interestingly, such elevated PGD_2 levels may also drive enhanced disease by interfering with the production of IFN-λ[57]. Both IFN-γ and IFN-λ treatments were already evaluated in various clinical settings. IFN-γ is licensed to treat chronic granulomatous disease[58] and is discussed as a treatment for idiopathic pulmonary fibrosis[59]. IFN-λ treatment was well tolerated by patients in the context of HCV infections[60-62], and a recent clinical trial demonstrated a marked efficacy in accelerating viral decline and clearance in SARS-CoV-2 infected patients[24]. Given the continuous burden of the currently ongoing and the threat of future pandemics, preparations should be taken to have broad-spectrum antivirals like type II and type III interferons accessible for the highly exposed and vulnerable if needed.

Material and Methods

Viruses and cell lines

The virus strain SARS-CoV-2 MA containing the amino acid changes Q498Y and P499T in the spike protein[37] has been generated by transformation-associated recombination in yeast as previously described[63]. Briefly, the mutations resulting in the Q498Y and P499T amino acid changes in the spike protein were generated in plasmids containing fragments 9 and 10 by using primers mSARSv3Fg9+10-F (5'-ATATGGTTTCtacacgACTAATGGTGTTGGTTAC) and mSARSv3Fg9+10-R (5'-GATTGTAAAGGAAAGTAACAATTAAAAC) by Q5 site-directed mutagenesis (New England Biolabs). Passage one SARS-CoV-2 MA stocks produced using Vero E6 cells were used in experiments. The identity of the resulting recombinant SARS-CoV-2 MA was confirmed by sequencing.

Plaque-purified virus stocks from passage 20 lung homogenates of passaging series DKO A and B were grown using Vero E6 cells. Plaque-purified virus stock derived from passaging series DKO A was plaque-purified a second time using Vero E6 cells to generate a SARS-CoV-2 MA20 virus stock for experiments. Briefly, virus stocks were produced by inoculating confluent Vero E6 cells with virus diluted in Opti-MEM (Gibco) 0.3 % BSA (Sigma-Aldrich) for 2 h at 37 °C with 5 % CO_2 after removal of cell culture medium (DMEM (Gibco) containing 10 % FCS (Anprotec), 20 U/ml penicillin, and 20 μg/mL streptomycin (Gibco)) and washing with PBS. After removal of infection medium, cells were washed with PBS and DMEM containing 2 % FCS and 20 mM HEPES (Roth) was added. After incubation for 48-72 h at 37 °C with 5 % CO_2, cell culture supernatants were harvested, cleared by centrifugation, aliquoted and stored at -80 °C until further use. Viral load in virus stocks was determined by plaque assay using Vero E6 cells. Purity of virus stocks was confirmed by next-generation sequencing. Sequenced B.1 (Muc-IMB-1/2020) and B.1.617.2 (Delta) virus stocks were provided by Georg Kochs[64].

African green monkey kidney Vero E6 cell line (ATCC CRL-1586) and human lung adenocarcinoma Calu-3 cell line (ATCC HTB-55) were purchased from ATCC. All virus infection experiments were performed under BSL-3 conditions.

Mice

C57BL/6JRj, BALB/cJRj and 129S2/SvPasOrlRj mice were purchased from Janvier Labs. B6.A2G-*Mx1,* B6.A2G-*Mx1-Ifnar1*$^{-/-}$, B6.A2G-*Mx1-Ifnlr1*$^{-/-}$, B6.AG2-*Mx1-Ifnar1*$^{-/-}$*Ifnlr1*$^{-/-}$, B6.*Ifngr1*$^{-/-}$, B6.*Ifnar1*$^{-/-}$*Ifngr1*$^{-/-}$, and B6.A2G-*Mx1-Stat1*$^{-/-}$ were bred and kept at the animal facilities of the University Medical Center Freiburg.

Mature adult 8- to 20-week-old mice, designated "adult", and middle-aged 36- to 60-week-old mice, designated "aged", were used in experiments. Animals of both sexes were used. All experimental groups were sex- and age-matched.

Infection of mice and IFN treatments

Mice were anaesthetized using 1.8-2.8 Vol % isoflurane in O_2 and subsequently inoculated with 40 μl PBS 0.1 % BSA containing the indicated dose of the respective virus variant via their nostrils. Infected mice were monitored daily for weight loss and clinical signs of disease for at least two weeks. Experimental end points when mice were euthanized by cervical dislocation were defined as ≥25 % weight loss or ≥20 % weight loss for longer than two days. To collect organ samples mice were euthanized by cervical dislocation. For histopathological analyses, mice were anaesthetized using ketamine/xylazine and fixed by transcardial perfusion with 10 % formalin solution and stored in 10 % formalin solution at 4 °C until further processing.

530 To determine viral loads by plaque assay, organs were homogenized 3-4 times in 800 μl PBS
531 at 6.5 m/s for 18 s using a FastPrep™ tissue homogenizer (MP Biomedicals). Homogenates
532 were centrifuged at 10 000 rpm for 10 min, supernatants collected and stored at -80 °C until
533 further processing.
534 Nasal swabs were collected using a wet cotton-swab and stored in 650 μl Opti-MEM 0.3 %
535 BSA at -80 °C. Samples were thawed at 20 °C with 1 400 rpm for 15 min on a thermoshaker
536 and viral load determined by plaque assay.
537 For intranasal treatment, isoflurane-anaesthetized mice were mock-treated with PBS 0.1 %
538 BSA or inoculated with the respective doses of IFN-$\alpha_{B/D}$[65] or human IFN-λ1/3[44] in a 40 μl
539 volume via their nostrils.
540 For subcutaneous treatment, mice were mock-treated with PBS 0.1 % BSA or injected with
541 the respective doses of human IFN-λ1/3, mouse IFN-γ or a combination of both in a 100 μl
542 volume using a 30 G syringe.

Plaque assay

543
544 Ten-fold serial dilutions of infectious samples were prepared in Opti-MEM 0.3 % BSA and
545 added to PBS-washed confluent Vero E6 cells, incubated for 2 h at 37 °C with 5 % CO_2 before
546 inoculum was removed, and cells overlaid with DMEM containing 0.1 % BSA, 1.5 % Avicel
547 (FMC BioPolymer), 0.5 mg/ml L-glutamine (Roth), 20 mM HEPES 20 U/ml penicillin, and 20
548 μg/mL streptomycin and incubated for 72 h at 37 °C with 5 % CO_2. After removal of Avicel
549 medium, cells were fixed using 10 % formalin solution and stained with 1 % crystal violet in
550 H_2O containing 20 % ethanol, each step for at least 25 min. Plaques were counted and used
551 to calculate virus titers defined as PFU per ml.
552 To plaque-purify clonal isolates, cells infected with serial dilutions were overlaid with DMEM
553 containing 2 % FCS, 0.6 % agar (Oxoid Germany), 0.01 % DEAE Dextran (Sigma), and 0.1 %
554 $NaHCO_3$ (Merck) and plaques picked 48-72 h p. i. using a thin filter-tip containing 2 μl PBS.

Cell culture, virus growth curves & plaque reduction neutralization test

555
556 Vero E6 and Calu-3 cells were cultured in DMEM and MEM, respectively, containing 10 %
557 FCS, 20 units/ml penicillin and 20 μg/mL streptomycin.
558 For virus growth curves, Vero E6 or Calu-3 cells seeded in 24-well plates were washed with
559 PBS and then infected with the respective virus strain by incubating the cells with virus
560 containing Opti-MEM 0.3 % BSA for 2 h at 37 °C with 5 % CO_2 using an MOI of 0.001. Cells
561 were washed with PBS and DMEM 2 % FCS added. Cell culture supernatants were collected
562 at the indicated time points and viral loads determined by plaque assay on Vero E6 cells.
563 Serological neutralization tests were performed using sera from vaccinated individuals 10- to
564 25-weeks post-vaccination with the second dose of Comirnaty (BioNTech/Pfizer) or Spikevax
565 (Moderna). Serial 2-fold dilutions of sera in Opti-MEM 0.3 % BSA were incubated for 1 h with
566 100 PFU of the indicated SARS-CoV-2 variant. The mixture was then added to Vero E6 cells
567 and incubated for 1.5 h at 37 °C with 5 % CO_2. After removal of the inoculum, cells were
568 overlaid with DMEM containing 2 % FCS, 0.6 % agar, 0.01 % DEAE Dextran, and 0.1 %
569 $NaHCO_3$ and incubated for 72 h at 37 °C with 5 % CO_2. Cells were fixed for 20 min using 10 %
570 formalin solution, stained for 20 min with 1 % crystal violet in H_2O containing 20 % ethanol
571 and plaques were counted. Plaque reduction was calculated relative to mock-treated
572 controls. 50 % neutralizing titers (NT50) were calculated by non-linear fit least squares
573 regression (constraints: 0 and 100).

RNA isolation and RT-qPCR

For RNA isolation, organ samples were homogenized four times in 800 µl TRI Reagent® (Zymo Research Corporation) at 6.5 m/s for 20 s using a FastPrep™ tissue homogenizer (MP Biomedicals). Samples were centrifuged at 10 000 rpm for 5 min and supernatant diluted in TRI Reagent® (1:2 to 1:32) was used for RNA extraction using the Direct-zol™ RNA Miniprep kit according to the manufacturer's instructions (Zymo Research Corporation).

cDNA was reverse-transcribed from 750 ng total RNA per sample using the LunaScript® RT SuperMix kit (New England Biolabs) and served as template for amplification of genes of interest (*Ubc*, QuantiTect® Primer Assay, Cat. No. QT00245189; *Tnf*, QuantiTect® Primer Assay, Cat. No. QT00104006; *Ifna4*, QuantiTect® Primer Assay, Cat. No. QT01774353; *Ifnl2/3*, Applied Biosystems, Cat. No. mm0420156_gH; *Ifnb1*, forward: 5'-CCTGGAGCAGCTGAATGGAA-3', reverse: 5'-CACTGTCTGCTGGTGGAGTTCATC-3', probe: 5'-[6FAM]CCTACAGGGCGGACTTCAAG[BHQ1]–3'; *Isg15*, forward: 5'-GAGCTAGAGCCTGCAGCAAT-3', reverse: 5'-TTCTGGGCAATCTGCTTCTT-3'; *Stat1*, forward: 5'-TCACAGTGGTTCGAGCTTCAG-3', reverse: 5'-CGAGACATCATAGGCAGCGTG-3'; *Mx1*, forward: 5'-TCTGAGGAGAGCCAGACGAT-3', reverse: 5'-ACTCTGGTCCCCAATGACAG-3'; *Il6*, forward: 5'-TCGGAGGCTTAATTACACATGTTCT-3', reverse: 5'-GCATCATCGTTGTTCATACAATCA-3') using SYBR™ Green PCR Master Mix (Applied Biosystems) or TaqMan® Universal PCR Master Mix (Qiagen) and a QuantStudio™ 5 Real-Time PCR System (Applied Biosystems). The increase in mRNA expression was determined by the $2^{-\Delta Ct}$ method relative to the expression of the indicated housekeeping gene.

Viral RNA was quantified by one-step RT-qPCR using the AgPath-ID™ One-Step RT-PCR (Applied Biosystems) reagents and the 2019-nCoV RT-qPCR primers (E_Sarbeco)[66] specific for the viral E gene. Serial dilutions of a defined RNA standard was used for absolute quantification as previously described[67].

Virus genome sequencing

RNA was extracted from 50 µl lung homogenate supernatant using the NucleoSpin® RNA Mini Kit according to the manufacturer's protocol (MACHEREY-NAGEL). cDNA was reverse-transcribed from extracted RNA using random hexamer primers and Superscript III (ThermoFisher) followed by PCR tiling of the entire SARS-CoV-2 genome (ARTIC V3 primer sets; https://github.com/artic-network/artic-ncov2019) producing ~400 bp long overlapping amplicons that were used to prepare the sequencing library. Amplicons were purified with AMPure magnetic beads (Beckman Coulter) and QIAseq FX DNA Library Kit (Qiagen) used to prepare indexed paired-end libraries for Illumina sequencing. Normalized and pooled sequencing libraries were denatured with 0.2 M NaOH. Libraries were sequenced on an Illumina MiSeq using the 300-cycle MiSeq Reagent Kit v2.

De-multiplexed raw reads were subjected to a customized Galaxy pipeline based on bioinformatics pipelines on usegalaxy.eu[68]. Raw reads were pre-processed with fastp v.0.20.1[69] and mapped to the SARS-CoV-2 Wuhan-Hu-1 reference genome (Genbank: NC_045512) using BWA-MEM v.0.7.17[70]. Primer sequences were trimmed using ivar trim v1.9 (https://andersen-lab.github.io/ivar/html/manualpage.html). Variants (SNPs and INDELs) were called using the ultrasensitive variant caller LoFreq v2.1.5[71], demanding a minimum base quality of 30 and a coverage ≥ 10-fold. Called variants were filtered based on a minimum variant frequency of 10 %. Effects of mutations were automatically annotated in vcf files using SnpEff v.4.3.1[72]. Consensus sequences were constructed using bcftools v.1.1.0[73]. Regions with low coverage (>20-fold) or variant frequencies between 30 and 70 % were masked with N.

621 A customized R script was used to plot variant frequencies that were detected by LoFreq as a
622 heatmap (github.com/jonas-fuchs/SARS-CoV-2-analyses) which is also available on
623 usegalaxy.eu ("Variant Frequency Plot").

624 **RNA-sequencing**
625 RNA was isolated from infected lungs as described above. RNA-sequencing was performed
626 on the HiSeq 4000 system (Illumina) with Single End 75 bp reads. Read quality trimming and
627 adaptor removal was carried out using Trimmomatic (version 0.36). The nf-core/rnaseq
628 pipeline (version 3.0;[74]) written in the Nextflow domain specific language (version 19.10.0;[75])
629 was used to perform the primary analysis of the samples in conjunction with Singularity
630 (version 2.6.0;[76]). All data was processed relative to the mouse GRCm38 genome
631 downloaded from Ensembl. Gene counts per gene per sample were obtained using the
632 RSEM-STAR ([77,78]) option of the pipeline and they were imported on DESeq (v1.28.0, [79])
633 within R environment v4.0.2 for differential expression analysis. Gene Ontology and Gene
634 Set Enrichment analysis (GSEA) were carried out using R package Cluster Profiler (v3.16). For
635 GSEA, gene lists ranked using the Wald statistic were used. Pre-ranked analyses were carried
636 out using C5 ontology GO biological process gene sets from the Molecular Signatures
637 database (MSigDB, v7.2). Gene signatures were considered significant if FDR q-value ≤ 0.05.
638 ggplot2, RColorBrewer, ComplexHeatmap were used for plotting purposes. Ingenuity
639 Pathway Analysis was performed using differentially expressed genes (fold change ≥ 1.5,
640 $p$adj ≤ 0.05). The indicated -log(p-values) were calculated using the Benjamini-Hochberg
641 method of multiple testing correction.

642 **Histopathology, immunohistochemistry, RNA in-situ-hybridization and scoring**
643 Mice, after cardiac perfusion as described above, were immersion-fixed with 10 % neutral-
644 buffered formalin solution. Tissue was embedded in paraffin, including the whole lung, 3-4
645 trimmed sections of the decalcified nasal cavity, a sagittal section of the brain, and a
646 longitudinal section of the heart. Samples were cut in 2-3-µm-thick sections and stained
647 with hematoxylin and eosin (HE) for light microscopical examination. Consecutive slides
648 were processed for immunohistochemistry (IHC). A polyclonal serum detecting the
649 nucleocapsid protein of SARS-CoV-2 (Rockland Immunochemicals # 200-401-A50, PA, USA)
650 was used according to standardized procedures of the avidin-biotin-peroxidase complex-
651 method (ABC, Vectastain Elite ABC Kit, Burlingame, CA, USA). Briefly, 2-3 µm sections were
652 mounted on adhesive glass slides, dewaxed in xylene, followed by rehydration in descending
653 graded alcohols. Endogenous peroxidase was quenched with 3 % hydrogen peroxide in
654 distilled water for 10 minutes at room temperature. Antigen heat retrieval was performed in
655 10 mM citrate buffer (pH 6) for 20 minutes in a pressure cooker. Nonspecific antibody
656 binding was blocked for 30 minutes at room temperature using normal goat serum, diluted
657 1:2 in PBS. The primary polyclonal serum was applied overnight at 4 °C (1:3000, diluted in
658 TRIS buffer), the secondary biotinylated goat anti-rabbit antibody was applied for 30 minutes
659 at room temperature (Vector Laboratories, Burlingame, CA, USA, 1:200). Color was
660 developed by incubating the slides with freshly prepared avidin-biotin-peroxidase complex
661 (ABC) solution (Vectastain Elite ABC Kit; Vector Laboratories), followed by exposure to 3-
662 amino-9-ethylcarbazole substrate (AEC, Dako, Carpinteria, CA, USA). Sections were
663 counterstained with Mayer's haematoxylin and coverslipped. As negative control, a
664 consecutive section was labelled with an irrelevant antibody detecting M protein of
665 Influenza A virus (ATCC clone HB-64) and a positive control slide was included in each run.
666 To validate RT-qPCR data, selected tissues (heart and brain) were tested with RNA in situ
667 hybridization (RNA ISH). The RNAScope 2-5 HD Reagent Kit-Red (ACD, Advanced Cell

668 Diagnostics, Newark, CA) was used as previously published[67]. For hybridization, RNAScope®
669 probes were custom-designed by ACD for SARS-CoV-2 nucleocapsid. The specificity of the
670 probes was verified using a positive control probe detecting RNA encoding for peptidylprolyl
671 isomerase B (cyclophilin B, ppib) and a negative control probe detecting RNA encoding for
672 dihydrodipicolinate reductase (DapB). In addition, to identify subtle inflammation in brain
673 and heart samples from infected 10-week (n=10) and 40-week-old (n=6) C57BL/6, hearts
674 were evaluated for the presence of CD3-positive T cell infiltrates and brains evaluated for
675 the presence of CD3-positive T cells and Iba-1-positive microglial cells/macrophages as
676 described in [80].
677 All sides were scanned using a Hamamatsu S60 scanner and evaluation was done using
678 NDPview.2 plus software (Version 2.8.24, Hamamatsu Photonics, K.K. Japan). The left lung
679 lobe was evaluated for histological changes based on HE staining applying criteria given in
680 **Supplementary Table S1**.
681 Following IHC, viral antigen was semi-quantitatively recorded in the nasal cavity on ordinal
682 scores using the tiers 0 = no antigen, score 1 = up to 3 foci, score 2 = more than 3 distinct
683 foci, score 3 = coalescing foci, score 4 = >80 % antigen positive. The left lung lobe was
684 evaluated using a 200 x 200 µm grid, positive grids were recorded, and the percentage of
685 positive grids was calculated. Target cells were identified based on the cellular phenotype
686 and their location as bronchial epithelium, alveolar macrophages, and alveolar epithelium,
687 including type 1 and type 2 pneumocytes. For heart and brain samples, IHC-based antigen
688 labeling as well as RNA ISH-based genome detection was recorded as present or absent.
689 Evaluation and interpretation were performed by a board-certified pathologist (DiplECVP) in
690 a masked fashion using the post-examination masking method[81].

691 **Ethics and biosafety**
692 The generation of recombinant SARS-CoV-2 MA was approved by the Swiss Federal Office for
693 Public Health (permission A202819).
694 All work performed at the University Medical Center Freiburg concerning virus isolation, cell
695 culture, and mouse infection experiments with infectious SARS-CoV-2 viruses was conducted
696 in Biosafety Level 3 (BSL-3) laboratories at the Institute of Virology, Freiburg, as approved by
697 the Regierungspräsidium Tübingen (#UNI.FRK.05.16-29). All animal work conducted at the
698 University Medical Center Freiburg and the Francis Crick Institute followed the German
699 animal protection law, or the Animals (Scientific Prpcedures) Act 1986, respectively, and was
700 approved by the respective local animal welfare committee (Regierungspräsidium Freiburg
701 #35-9185.81/G-20/91) or the UK Home Office London (Project Licence No. P9C468066).
702 Animal infection experiments were performed consistent with procedures of the Federation
703 for Laboratory Animal Science Associations and the national animal welfare body.

704 **Human samples**
705 Sera were obtained from eight vaccinees 10- to 25-weeks after a second dose of the
706 Comirnaty (BioN-TECH/Pfizer) or Spikevax (Moderna) vaccine. Written informed consent was
707 obtained from participants and the study was conducted according to federal guidelines and
708 local ethics committee regulations (Albert-Ludwigs-Universität, Freiburg, Germany: No. F-
709 2020-09-03-160428 and no. 322/20).

710 **Material, data and code Availability**
711 Material and reagents generated in this study will be made available upon installment of a
712 Material Transfer Agreement (MTA).

713   Genomic sequence of SARS-CoV-2 MA20, which was generated in this study, has been
714   deposited to _____. Passaging and plaque-purified deep sequencing data have been
715   uploaded to _____. RNA sequencing data are available in GEO under accession code
716   GSE190674.

717   **Statistical analyses**
718   Data visualization and analyses were performed using GraphPad Prism 9.0 and R version
719   3.5.1. Specific statistical tests, numbers of animals and / or replicates, and further definitions
720   of precision measures can be found in the respective figure legends or method details. *P*-
721   values are indicated in figures or figure legends.

Acknowledgements

References

1   O'Driscoll, M. *et al.* Age-specific mortality and immunity patterns of SARS-CoV-2. *Nature* **590**, 140-145, doi:10.1038/s41586-020-2918-0 (2021).

2   Zhang, Q. *et al.* Inborn errors of type I IFN immunity in patients with life-threatening COVID-19. *Science (New York, N.Y.)* **370**, doi:10.1126/science.abd4570 (2020).

3   Bastard, P. *et al.* Autoantibodies neutralizing type I IFNs are present in ~4% of uninfected individuals over 70 years old and account for ~20% of COVID-19 deaths. *Sci Immunol* **6**, doi:10.1126/sciimmunol.abl4340 (2021).

4   Bastard, P. *et al.* Autoantibodies against type I IFNs in patients with life-threatening COVID-19. *Science (New York, N.Y.)* **370**, doi:10.1126/science.abd4585 (2020).

5   Bartleson, J. M. *et al.* SARS-CoV-2, COVID-19 and the aging immune system. *Nature Aging* **1**, 769-782, doi:10.1038/s43587-021-00114-7 (2021).

6   Shaw, A. C., Goldstein, D. R. & Montgomery, R. R. Age-dependent dysregulation of innate immunity. *Nature reviews. Immunology* **13**, 875-887, doi:10.1038/nri3547 (2013).

7   Channappanavar, R. & Perlman, S. Age-related susceptibility to coronavirus infections: role of impaired and dysregulated host immunity. *The Journal of clinical investigation* **130**, 6204-6213, doi:10.1172/JCI144115 (2020).

8   Wong, L.-Y. R. & Perlman, S. Immune dysregulation and immunopathology induced by SARS-CoV-2 and related coronaviruses — are we our own worst enemy? *Nature Reviews Immunology* **22**, 47-56, doi:10.1038/s41577-021-00656-2 (2022).

9   Ye, L., Schnepf, D. & Staeheli, P. Interferon-λ orchestrates innate and adaptive mucosal immune responses. *Nature Reviews Immunology* **19**, 614-625, doi:10.1038/s41577-019-0182-z (2019).

10   Akamatsu, M. A., de Castro, J. T., Takano, C. Y. & Ho, P. L. Off balance: Interferons in COVID-19 lung infections. *EBioMedicine* **73**, 103642, doi:10.1016/j.ebiom.2021.103642 (2021).

11   Paludan, S. R. & Mogensen, T. H. Innate immunological pathways in COVID-19 pathogenesis. *Science Immunology* **7**, eabm5505, doi:doi:10.1126/sciimmunol.abm5505 (2022).

12   Park, A. & Iwasaki, A. Type I and Type III Interferons – Induction, Signaling, Evasion, and Application to Combat COVID-19. *Cell Host & Microbe* **27**, 870-878, doi:https://doi.org/10.1016/j.chom.2020.05.008 (2020).

13   Galani, I.-E. *et al.* Untuned antiviral immunity in COVID-19 revealed by temporal type I/III interferon patterns and flu comparison. *Nature Immunology* **22**, 32-40, doi:10.1038/s41590-020-00840-x (2021).

14   Hadjadj, J. *et al.* Impaired type I interferon activity and inflammatory responses in severe COVID-19 patients. *Science (New York, N.Y.)* **369**, 718-724, doi:10.1126/science.abc6027 (2020).

15   Meisel, C. *et al.* Mild COVID-19 despite autoantibodies against type I IFNs in autoimmune polyendocrine syndrome type 1. *The Journal of clinical investigation* **131**, doi:10.1172/JCI150867 (2021).

16   Loske, J. *et al.* Pre-activated antiviral innate immunity in the upper airways controls early SARS-CoV-2 infection in children. *Nature Biotechnology*, doi:10.1038/s41587-021-01037-9 (2021).

17   Yoshida, M. *et al.* Local and systemic responses to SARS-CoV-2 infection in children and adults. *Nature*, doi:10.1038/s41586-021-04345-x (2021).

788 18 Pekayvaz, K. *et al.* Protective immune trajectories in early viral containment of non-
789   pneumonic SARS-CoV-2 infection. *Nature Communications* **13**, 1018,
790   doi:10.1038/s41467-022-28508-0 (2022).
791 19 Wang, N. *et al.* Retrospective Multicenter Cohort Study Shows Early Interferon
792   Therapy Is Associated with Favorable Clinical Responses in COVID-19 Patients. *Cell*
793   *Host & Microbe* **28**, 455-464.e452, doi:https://doi.org/10.1016/j.chom.2020.07.005
794   (2020).
795 20 Davidson, S. *et al.* IFNλ is a potent anti-influenza therapeutic without the
796   inflammatory side effects of IFNα treatment. *EMBO molecular medicine* **8**, 1099-
797   1112, doi:10.15252/emmm.201606413 (2016).
798 21 Galani, I. E. *et al.* Interferon-λ Mediates Non-redundant Front-Line Antiviral
799   Protection against Influenza Virus Infection without Compromising Host Fitness.
800   *Immunity* **46**, 875-890.e876, doi:10.1016/j.immuni.2017.04.025 (2017).
801 22 Klinkhammer, J. *et al.* IFN-lambda prevents influenza virus spread from the upper
802   airways to the lungs and limits virus transmission. *Elife* **7**, doi:10.7554/eLife.33354
803   (2018).
804 23 Schnepf, D. *et al.* Selective Janus kinase inhibition preserves interferon-lambda-
805   mediated antiviral responses. *Sci Immunol* **6**, doi:10.1126/sciimmunol.abd5318
806   (2021).
807 24 Feld, J. J. *et al.* Peginterferon lambda for the treatment of outpatients with COVID-19:
808   a phase 2, placebo-controlled randomised trial. *The Lancet Respiratory Medicine* **9**,
809   498-510, doi:https://doi.org/10.1016/S2213-2600(20)30566-X (2021).
810 25 Heuberger, J. *et al.* Epithelial response to IFN-γ promotes SARS-CoV-2 infection.
811   *EMBO molecular medicine* **13**, e13191, doi:10.15252/emmm.202013191 (2021).
812 26 Busnadiego, I. *et al.* Antiviral Activity of Type I, II, and III Interferons Counterbalances
813   ACE2 Inducibility and Restricts SARS-CoV-2. *mBio* **11**, doi:10.1128/mBio.01928-20
814   (2020).
815 27 Witkowski, M. *et al.* Untimely TGFβ responses in COVID-19 limit antiviral functions of
816   NK cells. *Nature*, doi:10.1038/s41586-021-04142-6 (2021).
817 28 Krämer, B. *et al.* Early IFN-α signatures and persistent dysfunction are distinguishing
818   features of NK cells in severe COVID-19. *Immunity* **54**, 2650-2669.e2614,
819   doi:10.1016/j.immuni.2021.09.002 (2021).
820 29 Montagutelli, X. *et al.* Variants with the N501Y mutation extend SARS-CoV-2 host
821   range to mice, with contact transmission. *bioRxiv : the preprint server for biology*,
822   2021.2003.2018.436013, doi:10.1101/2021.03.18.436013 (2021).
823 30 Shuai, H. *et al.* Emerging SARS-CoV-2 variants expand species tropism to murines.
824   *EBioMedicine* **73**, 103643, doi:https://doi.org/10.1016/j.ebiom.2021.103643 (2021).
825 31 Zhou, B. *et al.* SARS-CoV-2 spike D614G change enhances replication and
826   transmission. *Nature* **592**, 122-127, doi:10.1038/s41586-021-03361-1 (2021).
827 32 Sun, S. H. *et al.* A Mouse Model of SARS-CoV-2 Infection and Pathogenesis. *Cell Host*
828   *Microbe* **28**, 124-133.e124, doi:10.1016/j.chom.2020.05.020 (2020).
829 33 Winkler, E. S. *et al.* SARS-CoV-2 Causes Lung Infection without Severe Disease in
830   Human ACE2 Knock-In Mice. *Journal of Virology* **96**, e01511-01521,
831   doi:doi:10.1128/JVI.01511-21 (2022).
832 34 Schepens, B. *et al.* An affinity-enhanced, broadly neutralizing heavy chain-only
833   antibody protects against SARS-CoV-2 infection in animal models. *Sci Transl Med* **13**,
834   eabi7826, doi:10.1126/scitranslmed.abi7826 (2021).

835 35 Wagner, T. R. *et al.* Biparatopic nanobodies protect mice from lethal challenge with
836 SARS-CoV-2 variants of concern. *EMBO Rep*, e53865, doi:10.15252/embr.202153865
837 (2021).

838 36 Winkler, E. S. *et al.* SARS-CoV-2 infection of human ACE2-transgenic mice causes
839 severe lung inflammation and impaired function. *Nature Immunology* **21**, 1327-1335,
840 doi:10.1038/s41590-020-0778-2 (2020).

841 37 Dinnon, K. H. *et al.* A mouse-adapted model of SARS-CoV-2 to test COVID-19
842 countermeasures. *Nature* **586**, 560-566, doi:10.1038/s41586-020-2708-8 (2020).

843 38 Gu, H. *et al.* Adaptation of SARS-CoV-2 in BALB/c mice for testing vaccine efficacy.
844 *Science (New York, N.Y.)* **369**, 1603-1607, doi:10.1126/science.abc4730 (2020).

845 39 Rathnasinghe, R. *et al.* The N501Y mutation in SARS-CoV-2 spike leads to morbidity in
846 obese and aged mice and is neutralized by convalescent and post-vaccination human
847 sera. *medRxiv : the preprint server for health sciences*,
848 doi:10.1101/2021.01.19.21249592 (2021).

849 40 Roy Wong, L.-Y. *et al.* Eicosanoid signaling as a therapeutic target in middle-aged
850 mice with severe COVID-19. *bioRxiv : the preprint server for biology*,
851 2021.2004.2020.440676, doi:10.1101/2021.04.20.440676 (2021).

852 41 Muruato, A. *et al.* Mouse-adapted SARS-CoV-2 protects animals from lethal SARS-CoV
853 challenge. *PLoS biology* **19**, e3001284, doi:10.1371/journal.pbio.3001284 (2021).

854 42 Gawish, R. *et al.* ACE2 is the critical in vivo receptor for SARS-CoV-2 in a novel COVID-
855 19 mouse model with TNF- and IFNγ-driven immunopathology. *Elife* **11**,
856 doi:10.7554/eLife.74623 (2022).

857 43 Leist, S. R. *et al.* A Mouse-Adapted SARS-CoV-2 Induces Acute Lung Injury and
858 Mortality in Standard Laboratory Mice. *Cell* **183**, 1070-1085.e1012,
859 doi:https://doi.org/10.1016/j.cell.2020.09.050 (2020).

860 44 Yu, D. *et al.* Design and evaluation of novel interferon lambda analogs with enhanced
861 antiviral activity and improved drug attributes. *Drug design, development and
862 therapy* **10**, 163-182, doi:10.2147/dddt.s91455 (2016).

863 45 Trinchieri, G. Interleukin-10 production by effector T cells: Th1 cells show self control.
864 *J Exp Med* **204**, 239-243, doi:10.1084/jem.20070104 (2007).

865 46 Couper, K. N., Blount, D. G. & Riley, E. M. IL-10: The Master Regulator of Immunity to
866 Infection. *The Journal of Immunology* **180**, 5771-5777,
867 doi:10.4049/jimmunol.180.9.5771 (2008).

868 47 Feld, J. J. *et al.* Peginterferon lambda for the treatment of outpatients with COVID-19:
869 a phase 2, placebo-controlled randomised trial. *The Lancet. Respiratory medicine* **9**,
870 498-510, doi:10.1016/s2213-2600(20)30566-x (2021).

871 48 Karki, R. & Kanneganti, T. D. The 'cytokine storm': molecular mechanisms and
872 therapeutic prospects. *Trends Immunol* **42**, 681-705, doi:10.1016/j.it.2021.06.001
873 (2021).

874 49 Fenimore, J. & Young, H. A. in *Regulation of Cytokine Gene Expression in Immunity
875 and Diseases* (ed Xiaojing Ma) 1-19 (Springer Netherlands, 2016).

876 50 Karki, R. *et al.* Synergism of TNF-α and IFN-γ Triggers Inflammatory Cell Death, Tissue
877 Damage, and Mortality in SARS-CoV-2 Infection and Cytokine Shock Syndromes. *Cell*
878 **184**, 149-168.e117, doi:https://doi.org/10.1016/j.cell.2020.11.025 (2021).

879 51 Broggi, A. *et al.* Type III interferons disrupt the lung epithelial barrier upon viral
880 recognition. *Science (New York, N.Y.)* **369**, 706-712, doi:10.1126/science.abc3545
881 (2020).

882   52   Major, J. *et al.* Type I and III interferons disrupt lung epithelial repair during recovery
883   from viral infection. *Science (New York, N.Y.)* **369**, 712-717,
884   doi:10.1126/science.abc2061 (2020).
885   53   Ye, L. *et al.* Interferon-λ enhances adaptive mucosal immunity by boosting release of
886   thymic stromal lymphopoietin. *Nat Immunol* **20**, 593-601, doi:10.1038/s41590-019-
887   0345-x (2019).
888   54   Roy Wong, L. Y. *et al.* Eicosanoid signaling as a therapeutic target in middle-aged mice
889   with severe COVID-19. *bioRxiv : the preprint server for biology*,
890   doi:10.1101/2021.04.20.440676 (2021).
891   55   Vijay, R. *et al.* Critical role of phospholipase A2 group IID in age-related susceptibility
892   to severe acute respiratory syndrome-CoV infection. *J Exp Med* **212**, 1851-1868,
893   doi:10.1084/jem.20150632 (2015).
894   56   Zhao, J., Zhao, J., Legge, K. & Perlman, S. Age-related increases in PGD(2) expression
895   impair respiratory DC migration, resulting in diminished T cell responses upon
896   respiratory virus infection in mice. *The Journal of clinical investigation* **121**, 4921-
897   4930, doi:10.1172/jci59777 (2011).
898   57   Werder, R. B. *et al.* PGD2/DP2 receptor activation promotes severe viral bronchiolitis
899   by suppressing IFN-λ production. *Sci Transl Med* **10**,
900   doi:10.1126/scitranslmed.aao0052 (2018).
901   58   Todd, P. A. & Goa, K. L. Interferon gamma-1b. A review of its pharmacology and
902   therapeutic potential in chronic granulomatous disease. *Drugs* **43**, 111-122,
903   doi:10.2165/00003495-199243010-00008 (1992).
904   59   Smaldone, G. C. Repurposing of gamma interferon via inhalation delivery. *Advanced
905   Drug Delivery Reviews* **133**, 87-92, doi:https://doi.org/10.1016/j.addr.2018.06.004
906   (2018).
907   60   Muir, A. J. *et al.* Phase 1b study of pegylated interferon lambda 1 with or without
908   ribavirin in patients with chronic genotype 1 hepatitis C virus infection. *Hepatology
909   (Baltimore, Md.)* **52**, 822-832, doi:10.1002/hep.23743 (2010).
910   61   Andersen, H. *et al.* Peginterferon Lambda-1a, a New Therapeutic for Hepatitis C
911   Infection, from Bench to Clinic. *Journal of clinical and translational hepatology* **1**, 116-
912   124, doi:10.14218/jcth.2013.00014 (2013).
913   62   Nelson, M. *et al.* Safety and Efficacy of Pegylated Interferon Lambda, Ribavirin, and
914   Daclatasvir in HCV and HIV-Coinfected Patients. *J Interferon Cytokine Res* **37**, 103-
915   111, doi:10.1089/jir.2016.0082 (2017).
916   63   Thi Nhu Thao, T. *et al.* Rapid reconstruction of SARS-CoV-2 using a synthetic genomics
917   platform. *Nature* **582**, 561-565, doi:10.1038/s41586-020-2294-9 (2020).
918   64   Tamara, K. *et al.* Antibody escape and global spread of SARS-CoV-2 lineage A.27.
919   *Nature Portfolio*, doi:10.21203/rs.3.rs-995033/v1 (2022).
920   65   Horisberger, M. A. & de Staritzky, K. A recombinant human interferon-alpha B/D
921   hybrid with a broad host-range. *The Journal of general virology* **68 (Pt 3)**, 945-948,
922   doi:10.1099/0022-1317-68-3-945 (1987).
923   66   Corman, V. M. *et al.* Detection of 2019 novel coronavirus (2019-nCoV) by real-time
924   RT-PCR. *Euro surveillance : bulletin Europeen sur les maladies transmissibles =
925   European communicable disease bulletin* **25**, doi:10.2807/1560-
926   7917.es.2020.25.3.2000045 (2020).
927   67   Schlottau, K. *et al.* SARS-CoV-2 in fruit bats, ferrets, pigs, and chickens: an
928   experimental transmission study. *The Lancet. Microbe* **1**, e218-e225,
929   doi:10.1016/s2666-5247(20)30089-6 (2020).

68   Kumar, A. B., A.H.; Gruening, B. . Community Research Amid COVID-19 Pandemic: Genomics Analysis of SARS-CoV-2 over Public GALAXY server. *Preprints*, doi:10.20944/preprints202005.0343.v1 (2020).

69   Chen, S., Zhou, Y., Chen, Y. & Gu, J. fastp: an ultra-fast all-in-one FASTQ preprocessor. *Bioinformatics* **34**, i884-i890, doi:10.1093/bioinformatics/bty560 (2018).

70   Li, H. & Durbin, R. Fast and accurate short read alignment with Burrows-Wheeler transform. *Bioinformatics* **25**, 1754-1760, doi:10.1093/bioinformatics/btp324 (2009).

71   Wilm, A. *et al.* LoFreq: a sequence-quality aware, ultra-sensitive variant caller for uncovering cell-population heterogeneity from high-throughput sequencing datasets. *Nucleic acids research* **40**, 11189-11201, doi:10.1093/nar/gks918 (2012).

72   Cingolani, P. *et al.* A program for annotating and predicting the effects of single nucleotide polymorphisms, SnpEff: SNPs in the genome of Drosophila melanogaster strain w1118; iso-2; iso-3. *Fly* **6**, 80-92, doi:10.4161/fly.19695 (2012).

73   Li, H. *et al.* The Sequence Alignment/Map format and SAMtools. *Bioinformatics* **25**, 2078-2079, doi:10.1093/bioinformatics/btp352 (2009).

74   Ewels, P. A. *et al.* The nf-core framework for community-curated bioinformatics pipelines. *Nat Biotechnol* **38**, 276-278, doi:10.1038/s41587-020-0439-x (2020).

75   Di Tommaso, P. *et al.* Nextflow enables reproducible computational workflows. *Nat Biotechnol* **35**, 316-319, doi:10.1038/nbt.3820 (2017).

76   Kurtzer, G. M., Sochat, V. & Bauer, M. W. Singularity: Scientific containers for mobility of compute. *PLoS One* **12**, e0177459, doi:10.1371/journal.pone.0177459 (2017).

77   Dobin, A. *et al.* STAR: ultrafast universal RNA-seq aligner. *Bioinformatics* **29**, 15-21, doi:10.1093/bioinformatics/bts635 (2013).

78   Li, B. & Dewey, C. N. RSEM: accurate transcript quantification from RNA-Seq data with or without a reference genome. *BMC Bioinformatics* **12**, 323, doi:10.1186/1471-2105-12-323 (2011).

79   Love, M. I., Huber, W. & Anders, S. Moderated estimation of fold change and dispersion for RNA-seq data with DESeq2. *Genome Biol* **15**, 550, doi:10.1186/s13059-014-0550-8 (2014).

80   Bennett, A. J. *et al.* Relatives of rubella virus in diverse mammals. *Nature* **586**, 424-428, doi:10.1038/s41586-020-2812-9 (2020).

81   Meyerholz, D. K. & Beck, A. P. Principles and approaches for reproducible scoring of tissue stains in research. *Laboratory Investigation* **98**, 844-855, doi:10.1038/s41374-018-0057-0 (2018).

Figure Legends

Figure 1 | Increased and prolonged replication of SARS-CoV-2 MA causes symptomatic disease in aged mice lacking type I and/or type III IFN receptors which correlates with an impaired immune response.

A) Groups of adult (8-18-week-old) mice of the indicated genotypes were infected with 10^5 PFU SARS-CoV-2 MA. Lungs were harvested at the indicated time points and viral loads determined by plaque assay on Vero E6 cells. Data pooled from five independent experiments. Symbols represent individual mice (n=4-13 per group) and bars indicate mean ± SEM. Dashed line indicates detection limit. *$P \leq 0.05$, **$P \leq 0.01$, ***$P \leq 0.001$, ****$P \leq 0.0001$, one-way ANOVA with Tukey's multiple comparisons test.

B) Groups of 16-24-week-old *Ifnlr1*$^{-/-}$ (triangles) and *Ifnar1*$^{-/-}$ mice (squares) were treated intranasally with the indicated doses of IFN-$\alpha_{B/D}$ or IFN-λ1/3, respectively, or mock-treated, one day after infection with 10^5 PFU SARS-CoV-2 MA. Lung viral loads on day 3 p. i. were determined by plaque assay on Vero E6 cells. Data from a single experiment are shown. Symbols represent individual mice (n=6-7 per group) and bars indicate mean ± SEM. Dashed line indicates detection limit. ****$P \leq 0.0001$, one-way ANOVA with Tukey's multiple comparisons test.

C-D) Groups of adult (10-15-week-old; n=7-8) (**C**) or aged (36-60-week-old mice; n=10-19) (**D**) of the indicated genotypes were infected with 10^5 PFU SARS-CoV-2 MA. Signs of disease and weight loss were monitored for 14 days. Data from a single experiment are shown in (**C**) and pooled data from two independent experiments are shown in (**D**). Symbols represent mean ± SEM. Dashed line indicates experimental endpoint due to animal welfare. Two-way ANOVA with Tukey's multiple comparisons test comparing WT with *Ifnar1*$^{-/-}$ (red), *Ifnlr1*$^{-/-}$ (blue) and *Ifnar1*$^{-/-}$*Ifnlr1*$^{-/-}$ (purple), **$P \leq 0.01$.

E) Groups of adult (8-12-week-old) or aged (40-60-week-old) mice (n=4-7) of the indicated genotypes were infected with 10^5 PFU SARS-CoV-2 MA. Lungs were harvested at the indicated time points and viral loads determined by plaque assay on Vero E6 cells. Data pooled from four independent experiments are shown. Symbols represent individual mice and bars indicate mean ± SEM. Dashed line indicates detection limit. *$P \leq 0.05$, **$P \leq 0.01$, unpaired t test.

F) Groups of adult (10-week-old) or aged (48-54-week-old) *Ifnar1*$^{-/-}$*Ifnlr1*$^{-/-}$ mice (n=5) of the indicated genotypes were infected with 10^5 PFU SARS-CoV-2 MA. Lungs were harvested on day 3 p. i. and viral RNA levels (*E* gene) were quantified by RT-qPCR. Data from a single experiment are shown. Symbols represent individual mice and bars indicate mean ± SEM. **$P \leq 0.01$, unpaired t test.

G-H) Groups of adult (12-week-old) or aged (44-week-old) *Ifnar1*$^{-/-}$ mice (n=5) were mock-infected (**G**) or infected with 10^5 PFU SARS-CoV-2 MA (**H**). Lungs were harvested on day 3 p. i. and processed for RNA sequencing. Gene Set Enrichment Analysis (GSEA) of ranked genes indicating strong enrichment for immune cell activation pathways in infected adult compared with aged mice. Negative and positive normalized enrichment scores (NES) indicate enrichment in aged and adult *Ifnar1*$^{-/-}$ mice, respectively. False Discovery Rate (FDR) < 10^{-2} for all pathways shown.

1006 **Figure 2 | Serial passaging of SARS-CoV-2 MA in *Ifnar1$^{-/-}$Ifnlr1$^{-/-}$* C57BL/6 mice yielded a**
1007 **highly virulent virus variant.**
1008 **A)** Schematic overview of serial passaging of SARS-CoV-2 MA in C57BL/6 (WT A and B) and
1009 B6-*Ifnar1$^{-/-}$Ifnlr1$^{-/-}$* mice (DKO A and B). Mice were initially infected with 10^5 PFU SARS-CoV-2
1010 MA. Serial passaging was performed by infecting mice with lung homogenates containing
1011 10^3-10^5 PFU. Lungs were harvested on day 3 post infection.
1012 **B)** Weight loss of C57BL/6 (WT A and B) and B6-*Ifnar1$^{-/-}$Ifnlr1$^{-/-}$* mice (DKO A and B) per
1013 passage on day 3 post infection. Symbols represent individual mice. Dashed line indicates
1014 experimental endpoint due to animal welfare.
1015 **C)** Weight loss (left panel) and survival (right panel) of adult C57BL/6 WT mice (8-10-week-
1016 old; n=5 per group) infected with diluted passage 20 (P20) lung homogenates derived from
1017 passaging series WT A, WT B, DKO A and DKO B containing 10^4 PFU. Data from a single
1018 experiment are shown. Symbols represent mean ± SEM. Dashed line indicates experimental
1019 endpoint due to animal welfare.
1020 **D)** Variant frequency plot from next-generation sequencing results for passaging series DKO
1021 A and the plaque-purified SARS-CoV-2 MA20 virus stock. Variant frequencies are shown in
1022 comparison to Wuhan-Hu-1 (NC_045512.2). Amino acid changes present in SARS-CoV-2
1023 MA20 are indicated in bold, changes in comparison to SARS-CoV-2 MA are highlighted in red.
1024 **E)** Comparative growth curves of SARS-CoV-2 strains B.1 and MA20 on Calu-3 cells infected
1025 with an MOI of 0.001. Virus replication was quantified by plaque assay on Vero E6 cells. Data
1026 from a single experiment performed in duplicates are shown. Dashed line indicates
1027 detection limit. **$P≤0.01$, ****$P≤0.0001$, two-way ANOVA with Tukey's multiple
1028 comparisons test.
1029 **F)** Weight loss (left panel) and survival (right panel) of adult C57BL/6 mice (10-14-week-old;
1030 n=5-10 per group) infected with the indicated dose of SARS-CoV-2 MA20. Pooled data from
1031 three independent experiments are shown. Symbols represent mean ± SEM. Dashed line
1032 indicates experimental endpoint due to animal welfare.
1033 **G)** Weight loss (left panel) and survival (right panel) of adult C57BL/6, 129/Sv or BALB/c mice
1034 (10-week-old; n=10 per group) infected with 10^3 PFU SARS-CoV-2 MA20. Data from a single
1035 experiment are shown. Symbols represent mean ± SEM. Dashed line indicates experimental
1036 endpoint due to animal welfare.

1037 **Figure 3 | SARS-CoV-2 MA20 efficiently replicates in upper airways and lungs of adult**
1038 **C57BL/6 mice inducing innate immune responses and tissue damage.**
1039 **A-J**) Adult C57BL/6 mice (8-17-week-old; n=4-8 per group) were mock-treated or infected
1040 with 10^3 PFU SARS-CoV-2 MA20. Samples were collected at the indicated time points.
1041 (**A**) Nasal swabs were taken at the indicated time points and viral loads determined by
1042 plaque assay on Vero E6 cells. Symbols represent individual mice and bars indicate mean ±
1043 SEM. Dashed line indicates detection limit.
1044 (**B**) Viral replication in upper airways was quantified as SARS-CoV-2 genome equivalents per
1045 ml by measuring expression levels of the viral gene *E* by RT-qPCR at the indicated time
1046 points. Symbols represent individual mice and bars indicate mean ± SEM.
1047 (**C**) Viral load in lungs was determined by plaque assay on Vero E6 cells at the indicated time
1048 points. Symbols represent individual mice and bars indicate mean ± SEM. Dashed line
1049 indicates detection limit.
1050 (**D**) Gene expression levels of *Il6*, *Tnf*, *Ifna4*, *Ifnb*, *Ifnl2/3*, *Mx1*, *Isg15* and *Stat1* in lungs were
1051 determined relative to *Ubc* by RT-qPCR. Symbols represent mean ± SD.
1052 **E-I**) Mice were prepared for histological analyses by cardiac perfusion at the indicated time
1053 points. (**E**) Representative pictures for histopathology and immunohistochemistry are
1054 shown. Bar indicates 50 μm. Antigen (**F**) and histopathologic lesion scores for lungs (**G**) and
1055 necrotizing bronchitis (**H**) and regeneration scores (**I**) were quantified as described in
1056 materials and methods section.
1057 (**J**) Viral RNA levels in lung, heart, liver, intestine, kidney, spleen and brain was quantified as
1058 SARS-CoV-2 genome equivalents per ml by measuring expression levels of the viral gene *E* by
1059 RT-qPCR at the indicated time points. Symbols represent individual mice and bars indicate
1060 mean ± SEM. Dashed line indicates detection limit.

1061 **Figure 4 | Enhanced susceptibility of aged mice to SARS-CoV-2-induced disease correlates**
1062 **with increased viral load.**
1063 **A-I**) Groups of adult or aged (10-week- or 40-week-old) C57BL/6 mice were infected with 300
1064 PFU SARS-CoV-2 MA20. Subgroups of mice were sacrificed at the indicated time points to
1065 quantify virus replication and to evaluate virus-induced tissue damage.
1066 **A**) Weight loss (left panel) and survival (right panel) was monitored for 14 days post
1067 infection. Data from a single experiment are shown. Symbols represent mean ± SEM. Dashed
1068 line indicates experimental endpoint due to animal welfare. Survival: **$P \le 0.01$, Log-rank
1069 (Mantel-Cox) test, n = 5 per group.
1070 **B**) Viral replication in upper airways was quantified as SARS-CoV-2 genome equivalents per
1071 ml by measuring expression levels of the viral gene *E* by RT-qPCR at the indicated time
1072 points. Data from a single experiment are shown. Symbols represent individual mice and
1073 bars indicate mean ± SEM. *$P \le 0.05$, ****$P \le 0.0001$, one-way ANOVA with Tukey's multiple
1074 comparisons test, n = 3-5 per group.
1075 **C**) Viral load in lungs was determined by plaque assay on Vero E6 cells at the indicated time
1076 points. Data from a single experiment are shown. Symbols represent individual mice and
1077 bars indicate mean ± SEM. Dashed line indicates detection limit. *$P \le 0.05$, ****$P \le 0.0001$,
1078 one-way ANOVA with Tukey's multiple comparisons test, n = 3-5 per group.
1079 **D-H**) Groups of mice (n = 2-5) were prepared for histological analyses by cardiac perfusion at
1080 the indicated time points. (**D**) Representative pictures for histopathology and
1081 immunohistochemistry are shown. Bar indicates 50 μm. Antigen (**E**) and histopathologic
1082 lesion scores for lungs (**F**), necrotizing bronchitis (**G**) and regeneration scores (**H**) were
1083 quantified as described in materials and methods section.
1084 **I**) Viral RNA in lungs, heart, liver, intestine, kidney, spleen and brain was quantified as SARS-
1085 CoV-2 genome equivalents per ml by measuring expression levels of the viral gene *E* by RT-
1086 qPCR at the indicated time points. Symbols represent individual mice and bars indicate mean
1087 ± SEM. Dashed line indicates detection limit. *$P \le 0.05$, **$P \le 0.01$, ***$P \le 0.001$, one-way
1088 ANOVA with Tukey's multiple comparisons test, n = 3-5 per group.

1089 **Figure 5 | Immune response in SARS-CoV-2 infected aged mice is delayed, diminished and**
1090 **dysregulated.**
1091 **A-C**) Groups of adult or aged (10-week- or 40-week-old) C57BL/6 mice (n=3-5 per group)
1092 were infected with 300 PFU SARS-CoV-2 MA20. Lungs were harvested at the indicated time
1093 points, processed and subjected to RNA sequencing.
1094 **A**) Principal component analysis (PCA) plot of RNA-sequencing data obtained from total
1095 lungs of the indicated groups of mice.
1096 **B**) Gene Set Enrichment Analyses (GSEA) comparing adult and aged mice at each time point
1097 post infection. Gene set pre-ranked analyses were carried out using the C5 gene ontology
1098 (GO) gene set collection in the Molecular Signatures Database (MSigDB).
1099 **C**) Heat map for significant differences in Canonical Pathways as defined by Ingenuity
1100 Pathway Analysis (IPA). Six pairwise comparisons between infected lung samples and their
1101 respective mock controls, from adult or aged animals, at the indicated days p. i., are shown
1102 (fold change >1.5, *p*adj < 0.05). The Benjamini-Hochberg method of multiple testing
1103 correction was used to calculate -log(p-values). Up- and down-regulated transcripts across
1104 the different pairwise comparisons in the "Th1 and Th2 pathway" are shown as heat map.

Figure 6 | Combined deficiency in type I and type II IFN signaling phenocopies age-dependent disease susceptibility.

A) Adult (8-20-week-old) WT, $Ifnar1^{-/-}$, $Ifnlr1^{-/-}$ and $Ifnar1^{-/-}Ifnlr1^{-/-}$ mice (n=15-16) were infected with 300 PFU SARS-CoV-2 MA20. Weight loss (upper panel) and survival (lower panel) was monitored for 14 days post infection. Data pooled from two independent experiments. Dashed line indicates experimental endpoint due to animal welfare. Symbols represent mean ± SEM. Weight loss: p-values for WT in comparison with $Ifnar1^{-/-}$ (red), $Ifnlr1^{-/-}$ (blue) and $Ifnar1^{-/-}Ifnlr1^{-/-}$ (purple) by two-way ANOVA with Tukey's multiple comparisons test. Survival: ****$P \le 0.0001$, Log-rank (Mantel-Cox) test.

B-H) Groups of adult or aged (10-20-week- or 38-60-week-old) mice of the indicated genotypes were infected with 30 PFU SARS-CoV-2 MA20. Weight loss (upper panel) and survival (lower panel) was monitored for 14 days post infection. Dashed line indicates experimental endpoint due to animal welfare. Weight loss: p-values calculated by two-way ANOVA with Šídák's multiple comparisons test. Survival: *$P \le 0.05$, ****$P \le 0.0001$, Log-rank (Mantel-Cox) test. (**B-E**) All mice were infected in parallel and data from a single experiment are shown; n=5-9. (**F**) Data pooled from three independent experiments; n=18-20. (**G**) Data pooled from two independent experiments; n=11-15. (**H**) Data pooled from two independent experiments; n=17.

Figure 7 | Therapeutic administration of IFN-λ prevents SARS-CoV-2-induced lethality in absence of type I IFN immunity and supplementation of IFN-γ reverses age-dependent disease phenotype

A) Groups of adult *Ifnar1*$^{-/-}$ mice (9-15-week-old) were either mock-treated (n=12), treated prophylactically by subcutaneous injection of 2 µg IFN-λ1/3 once one day prior to infection (n=6), or treated therapeutically with 3 µg IFN-λ1/3 daily for one week (n=8) starting one day after infection with 1000 PFU SARS-CoV-2 MA20. Dashed line indicates experimental endpoint due to animal welfare. Pooled data from two independent experiments are shown. Symbols represent mean ± SEM. Weight loss: mock in comparison with prophylactic (asterisks) or therapeutic (hashes) by two-way ANOVA with Tukey's multiple comparisons test; *$P \leq 0.05$, #$P \leq 0.05$, ****$P \leq 0.0001$, ####$P \leq 0.0001$. Survival: Log-rank (Mantel-Cox) test; **$P \leq 0.01$.

B) Groups of aged *Ifnar1*$^{-/-}$ (49-60-week-old) mice were either mock-treated (n=12), treated prophylactically by subcutaneous injection of 3 µg IFN-λ1/3 once one day prior to infection (n=6), or treated therapeutically with 3 µg IFN-λ1/3 daily for one week (n=8) starting one day after infection with 100 PFU SARS-CoV-2 MA20. Dashed line indicates experimental endpoint due to animal welfare. Pooled data from two independent experiments are shown. Symbols represent mean ± SEM. Weight loss: mock in comparison with therapeutic by two-way ANOVA with Tukey's multiple comparisons test; *$P \leq 0.05$, **$P \leq 0.01$. Survival: Log-rank (Mantel-Cox) test.

C) Groups of aged WT mice (45-52-week-old) were either mock-treated (n=8) or treated subcutaneously with 2 µg IFN-γ daily (n=8) for nine days starting one day prior to infection with 200 PFU SARS-CoV-2 MA20. Infected but untreated adult WT mice (10-16-week-old; n=8) served as controls. Dashed line indicates experimental endpoint due to animal welfare. Data from a single experiment are shown. Symbols represent mean ± SEM. Weight loss: $P \leq 0.05$ for mock-treated aged mice in comparison with adult control mice (black) or with IFN-γ-treated aged mice (orange) by two-way ANOVA with Tukey's multiple comparisons test; **$P \leq 0.01$ comparing adult control mice with IFN-γ-treated aged mice. Survival: Log-rank (Mantel-Cox) test, *$P \leq 0.05$.

D) Groups of aged *Ifnar1*$^{-/-}$ mice (52-60-week-old) were either mock-treated (n=9) or treated therapeutically with a mixture of 3 µg IFN-λ1/3 and 3 µg IFN-γ daily for one week (n=8), starting one day after infection with 100 PFU SARS-CoV-2 MA20. Dashed line indicates experimental endpoint due to animal welfare. Data from a single experiment are shown. Symbols represent mean ± SEM. Weight loss: mock in comparison with therapeutic treatment group by two-way ANOVA with Šídák's multiple comparisons test; ****$P \leq 0.0001$. Survival: Log-rank (Mantel-Cox) test; ****$P \leq 0.0001$.

Figure S1 | Increased and prolonged replication of SARS-CoV-2 MA in mice lacking type I and/or type III IFN receptors.

A) Groups of adult mice (8-18-week-old) of the indicated genotypes were infected with 10^5 PFU SARS-CoV-2 MA. Upper airways were harvested at the indicated time points and viral load determined by plaque assay on Vero E6 cells. Data pooled from five independent experiments. Symbols represent individual mice (n=4-13 per group) and bars indicate mean ± SEM. Dashed line indicates detection limit. *$P≤0.05$, **$P≤0.01$, ***$P≤0.001$, ****$P≤0.0001$, one-way ANOVA with Tukey's multiple comparisons test.

B) Groups of 16-24 week-old *Ifnlr1*$^{-/-}$ (triangles) and *Ifnar1*$^{-/-}$ mice (squares) were intranasally treated with the indicated dose of IFN-$\alpha_{B/D}$ or IFN-λ1/3, respectively, or mock-treated one day prior to infection with 10^5 PFU SARS-CoV-2 MA. Lung viral loads on day 3 p. i. were determined by plaque assay on Vero E6 cells. Data from a single experiment are shown. Symbols represent individual mice (n=6-7 per group) and bars indicate mean ± SEM. Dashed line indicates detection limit. ****$P≤0.0001$, one-way ANOVA with Tukey's multiple comparisons test.

C-F) Groups of adult (8-10-week-old) WT or *Ifnar1*$^{-/-}$ *Ifnlr1*$^{-/-}$ mice were mock-treated or infected with 10^5 PFU SARS-CoV-2 MA (n=2-3 per group) and prepared for histological analyses by cardiac perfusion. Antigen and histopathologic lesion scores for lungs and necrotizing bronchitis were quantified as described in materials and methods section. Data pooled from two independent experiments are shown. Symbols represent individual mice and bars indicate mean ± SEM.

G) Survival graph corresponding to Figure 1D.

H-J) Groups of adult (8-10-week-old; n=4) or aged *Ifnar1*$^{-/-}$ mice (36-52-week-old; n=5) were infected with 10^5 PFU SARS-CoV-2 MA. Mice were prepared for histological analyses by cardiac perfusion on day three post infection. Antigen and histopathologic lesion scores for bronchial necrosis were quantified as described in materials and methods section. *$P≤0.05$, **$P≤0.01$, unpaired t test.

K) Groups of adult or aged mice (8-12-week- or 40-60-week-old; n=4-7) of the indicated genotypes were infected with 10^5 PFU SARS-CoV-2 MA. Upper airways were harvested at the indicated time points and viral loads determined by plaque assay on Vero E6 cells. Data pooled from four independent experiments are shown. Symbols represent individual mice and bars indicate mean ± SEM. Dashed line indicates detection limit. *$P≤0.05$, unpaired t test.

Figure S2 | Serial passaging of MA SARS-CoV-2 in IFN receptor-deficient C57BL/6 mice allows for rapid host adaptation.

A-B) Viral load on day 3 p. i. in upper airways (**A**) and lungs (**B**) for passaging series WT A, WT B, DKO A and DKO B determined by plaque assay on Vero E6 cells. Dashed line indicates detection limit.

C) Weight loss (left panel) and survival (right panel) of adult C57BL/6 WT mice (13-15-week-old; n=6 per group) infected with 5×10^3 PFU of plaque-purified virus stocks DKO A PP and DKO B PP. Data from a single experiment are shown. Symbols represent individual mice and bars indicate mean ± SEM. Dashed line indicates experimental endpoint due to animal welfare. ******$P \leq 0.01$, *******$P \leq 0.001$, two-way ANOVA with Šídák's multiple comparisons test.

D) Variant frequency plot from next-generation sequencing results for the passaging series DKO B and the plaque-purified "DKO B PP" virus stock. Variant frequencies are shown in comparison to Wuhan-Hu-1 (NC_045512.2). Amino acid changes present in DKO B PP are indicated in bold, changes in comparison to SARS-CoV-2 MA are highlighted in red.

E) Table indicating similar (orange) or identical (green) amino acid changes present in SARS-CoV-2 MA10, SARS2-N501$_{MA30}$, B1-1-529 (Omicron), B.1.351 (Beta) and P.1 (Gamma) in comparison with amino acid changes present in SARS-CoV-2 MA20 (red). Reference sequence: Wuhan-Hu-1 (NC_045512.2). Amino acid changes highlighted in grey were already present in SARS-CoV-2 MA.

F) Comparative growth curves of B.1 and SARS-CoV-2 MA20 on VeroE6 cells infected with an MOI of 0.001. Virus replication was quantified by plaque assay on Vero E6 cells. Data from a single experiment performed in duplicates are shown. Dashed line indicates detection limit. ******$P \leq 0.01$, two-way ANOVA with Tukey's multiple comparisons test.

G) Comparative neutralization by plaque reduction neutralization test of SARS-CoV-2 MA20 and B.1.617.2 (Delta) using sera from vaccinated individuals. Symbols represent mean value for each individual determined in three independent assays. *******$P \leq 0.001$, paired t test.

H) Adult C57BL/6 mice (10-week-old; n=5 per group) were infected with 10^3 PFU of SARS-CoV-2 MA20. Upper airways were harvested at the indicated time points and gene expression levels of *Il6*, *Tnf*, *Ifna4*, *Ifnb*, *Ifnl2/3*, *Mx1*, *Isg15* and *Stat1* were determined relative to *Ubc* by RT-qPCR. Symbols represent mean ± SD.

1222 **Figure S3 | Therapeutic administration of IFN-λ or IFN-γ reduces SARS-CoV-2 induced**
1223 **lethality in aged mice.**
1224 **A**) Groups of adult or aged C57BL/6 (10-week- or 40-week-old; n = 5 per group) were
1225 infected with 100 PFU SARS-CoV-2 MA20. Weight loss (left panel) and survival (right panel)
1226 were monitored for 14 days post infection. Data from a single experiment are shown.
1227 Symbols represent mean ± SEM. Dashed line indicates experimental endpoint due to animal
1228 welfare. Survival: **$P \leq 0.01$, Log-rank (Mantel-Cox) test. Dataset for infected 10-week-old
1229 mice is also blotted in Figure 2G.
1230 **B**) Groups of aged WT mice (45-56-week-old) were either mock-treated (n=8) or treated
1231 therapeutically with 3 µg IFN-λ1/3 (n=8) daily for one week starting one day after infection
1232 with 200 PFU SARS-CoV-2 MA20. Mock-treated control group is the same as depicted in
1233 Figure 7C. Data from a single experiment are shown. Dashed line indicates experimental
1234 endpoint due to animal welfare. Symbols represent mean ± SEM. Weight loss: $P \leq 0.05$ by
1235 two-way ANOVA with Šídák's multiple comparisons test. Survival: Log-rank (Mantel-Cox)
1236 test, *$P \leq 0.05$.
1237 **C**) Groups of aged *Ifnar1*^{-/-} mice (52-60-week-old) were either mock-treated (n=9) or treated
1238 therapeutically by subcutaneous injection of 3 µg IFN-γ daily for one week (n=8) starting one
1239 day after infection with 100 PFU SARS-CoV-2 MA20. Mock-treated control group is the same
1240 as depicted in Figure 6D. Data from a single experiment are shown. Dashed line indicates
1241 experimental endpoint due to animal welfare. Survival: Log-rank (Mantel-Cox) test, *$P \leq 0.05$.


1242 **Figure S4 | Impaired immune response drives age-dependent virulence of SARS-CoV-2**
1243 Graphical summary illustrating the age-dependent impairment of immune responses and
1244 suggested intervention strategies.

1245 **Supplementary Table S1:** Histological scoring criteria

Criteria no.	Criteria	Scoring description*
1	atelectasis (pneumonia-associated), area affected	0 = no change, 1 = focal to oligofocal <5%, 2 = multifocal (6-40%), 3 = coalescing (41-80%), 4 = diffuse >80%
2	infiltrates alveolar, area affected	0 = no change, 1 = focal to oligofocal <5%, 2 = multifocal (6-40%), 3 = coalescing (41-80%), 4 = diffuse >80%
3	infiltrates alveolar, grade	0 = no infiltrates, 1 = 1-2 cells, 2 = 2-3 cells, 3 = almost filling, 4 = full atelektasis, grade is representative for the lobe
	description: predominant cell type	granulocytes, lymphocytes, macrophages, plasma cells, mixture (no predominant cell type)
4	infiltrates interstitial, area affected	0 = no change, 1 = focal to oligofocal <5%, 2 = multifocal (6-40%), 3 = coalescing (41-80%), 4 = diffuse >80%
5	infiltrates interstitial, grade	0 = no infiltrates, 1 = subtle, 2 = thickend septa but regular alveolar pattern, 3 = thickened septa partially obscured alveolar architecture, 4 = full atelektasis; grade is representative for lobe
	description: predominant cell type	granulocytes, lymphocytes, macrophages, plasma cells, mixture (no predominant cell type)
6	infiltrates peribronchial (incl glands), occurence	0 = not present, 1 = present in 1-3 foci, 3 = significantly present in >3 foci
7	infiltrates peribronchial, grade	= cell layers; 1=1, 2=2-3, 3=4-5, 4≥6 give max grade
	description: predominant cell type	granulocytes, lymphocytes, macrophages, plasma cells, mixture (no predominant cell type)
8	necrotizing bronchitis, occurence	0 = not present, 1 = present in 1-3 foci, 3 = significantly present in >3 foci
9	necrotizing bronchitis, grade	for infiltrates /debris(1=few cells, 2 aggregates, 3 almost filling; 4 > filling lumen), grade max
	description: predominant cell type	granulocytes, lymphocytes, macrophages, plasma cells, mixture (no predominant cell type)
10	Mucus increased	main = 1; periphery = 2
11	infiltrates perivascular, occurence	0 = not present, 1 = present in 1-3 foci, 3 = significantly present in >3 foci
12	infiltrates perivascular, grade	0 = no infiltrates, 1 = 1 cell layer, 2 = 2-3 layers, 3 = 4-5 layers, 4 = ≥6 layers, maximum score given
	description: predominant cell type	granulocytes, lymphocytes, macrophages, plasma cells, mixture (no predominant cell type)
13	vascular rolling of immune cell, occurence	0 = not present, 1 = present in 1-3 foci, 3 = significantly present in >3 foci
14	endotheliitis, occurence	0 = not present, 1 = present in 1-3 foci, 3 = significantly present in >3 foci
15	vasculitis, i.e. mural damage, transmigrating immune cells	0 = not present, 1 = present in 1-3 foci, 3 = significantly present in >3 foci
16	thrombi, occurence	0 = not present, 1 = present
17	necrosis, alveolar epithelium, area affected	0 = no change, 1 = focal to oligofocal <5%, 2 = multifocal (6-40%), 3 = coalescing (41-80%), 4 = diffuse >80%
18	diffuse alveolar damage, with hyaline membrane, debris, fibrin, area affected	0 = no change, 1 = focal to oligofocal <5%, 2 = multifocal (6-40%), 3 = coalescing (41-80%), 4 = diffuse >80%
19	hypertrophy/hyperplasia, bronchi, occurence	0 = not present, 1 = present in 1-3 foci, 3 = significantly present in >3 foci
20	hyperplasia /hypertrophy type II pneumocytes, area affected	0 = no change, 1 = focal to oligofocal <5%, 2 = multifocal (6-40%), 3 = coalescing (41-80%), 4 = diffuse >80%
21	atypical cells or syncytia, occurence	0 = not present, 1 = present
sum scores	**bronchial necrosis**	**sum of no. 8 to 9**
	necrotizing bronchitis	**sum of no. 6 to 9**
	regeneration	**sum of no. 19 to 20**
	total lung score	**sum of no. 1 to 21**

1246 *scores can be translated to minimal (score 1), mild (score 2), moderate (score 3), severe (score 4)
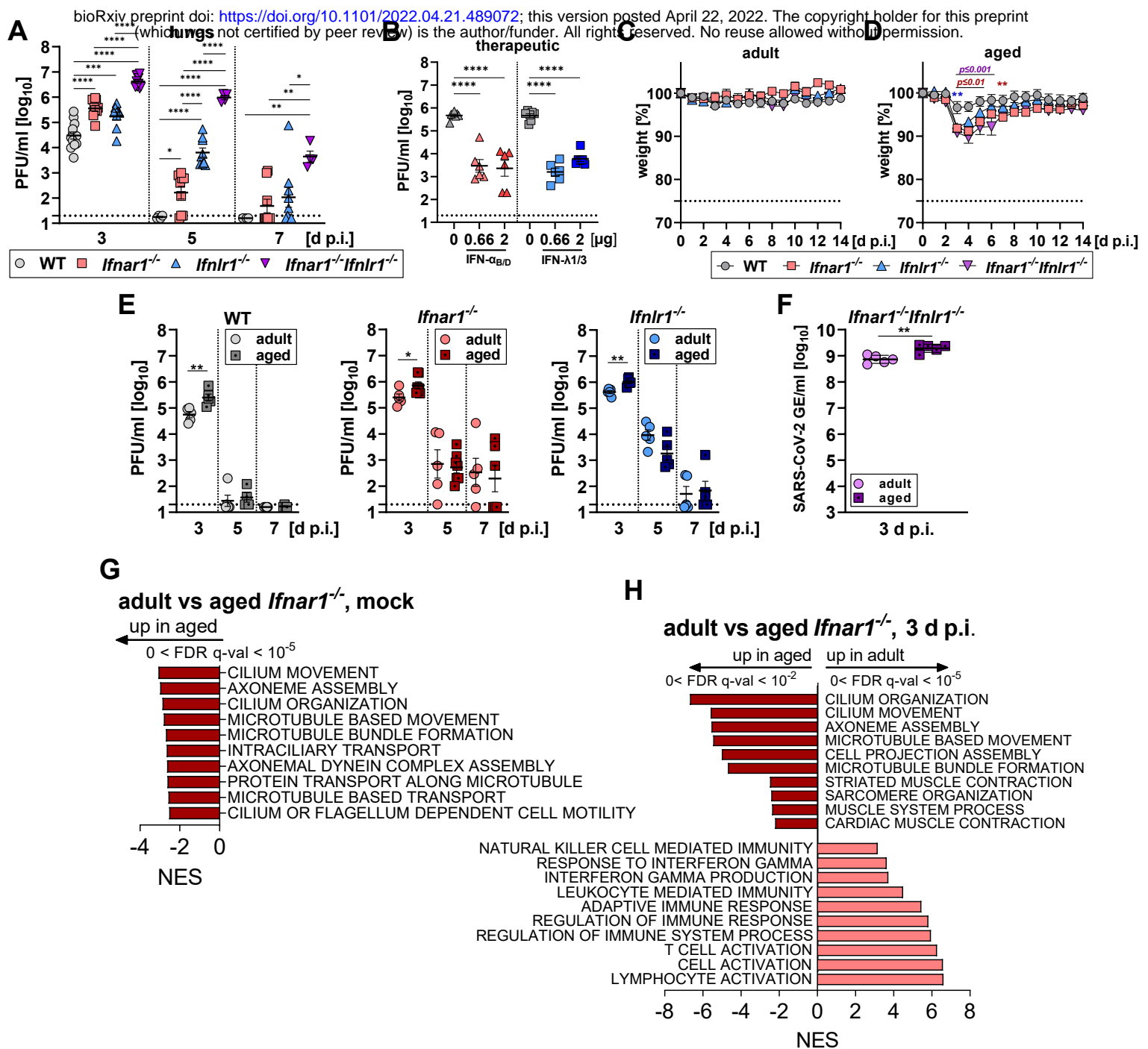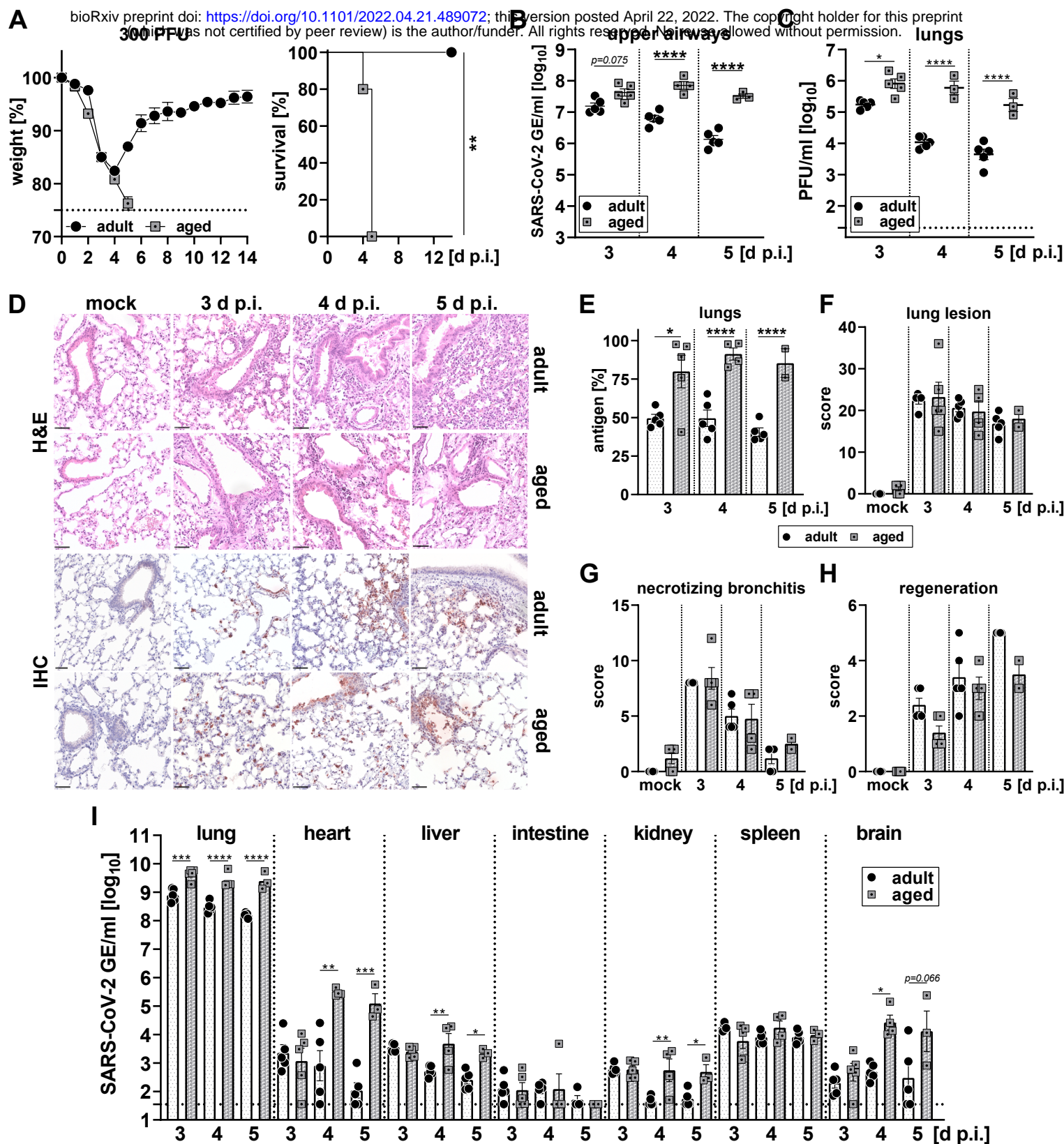
Figure 1 | Increased and prolonged replication of SARS-CoV-2 MA causes symptomatic disease in aged mice lacking type I and/or type III IFN receptors which correlates with an impaired immune response.
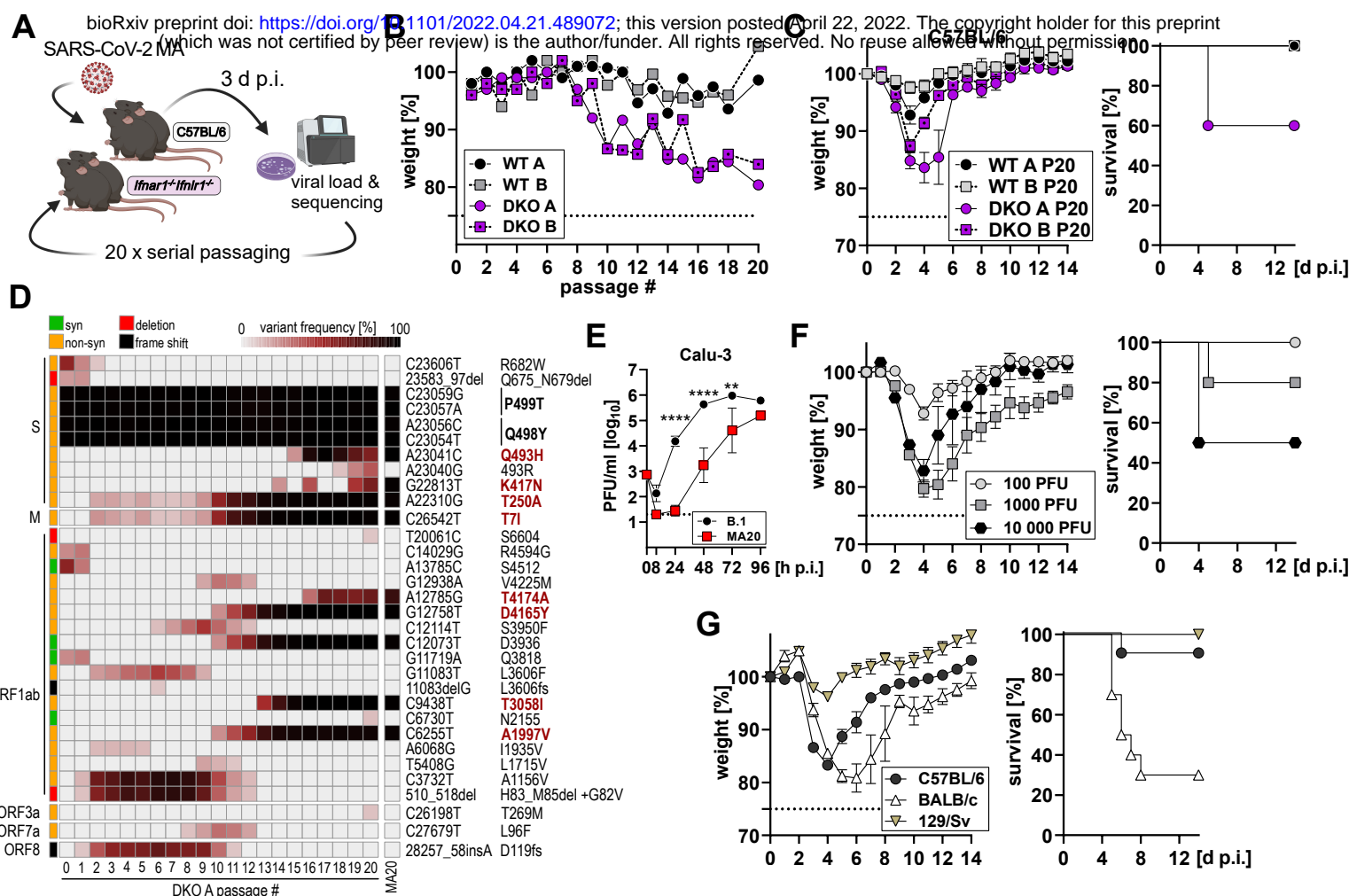
Figure 2 | Serial passaging of SARS-CoV-2 MA in *Ifnar1-/-Ifnlr1-/-* C57BL/6 mice yielded a highly virulent virus variant.
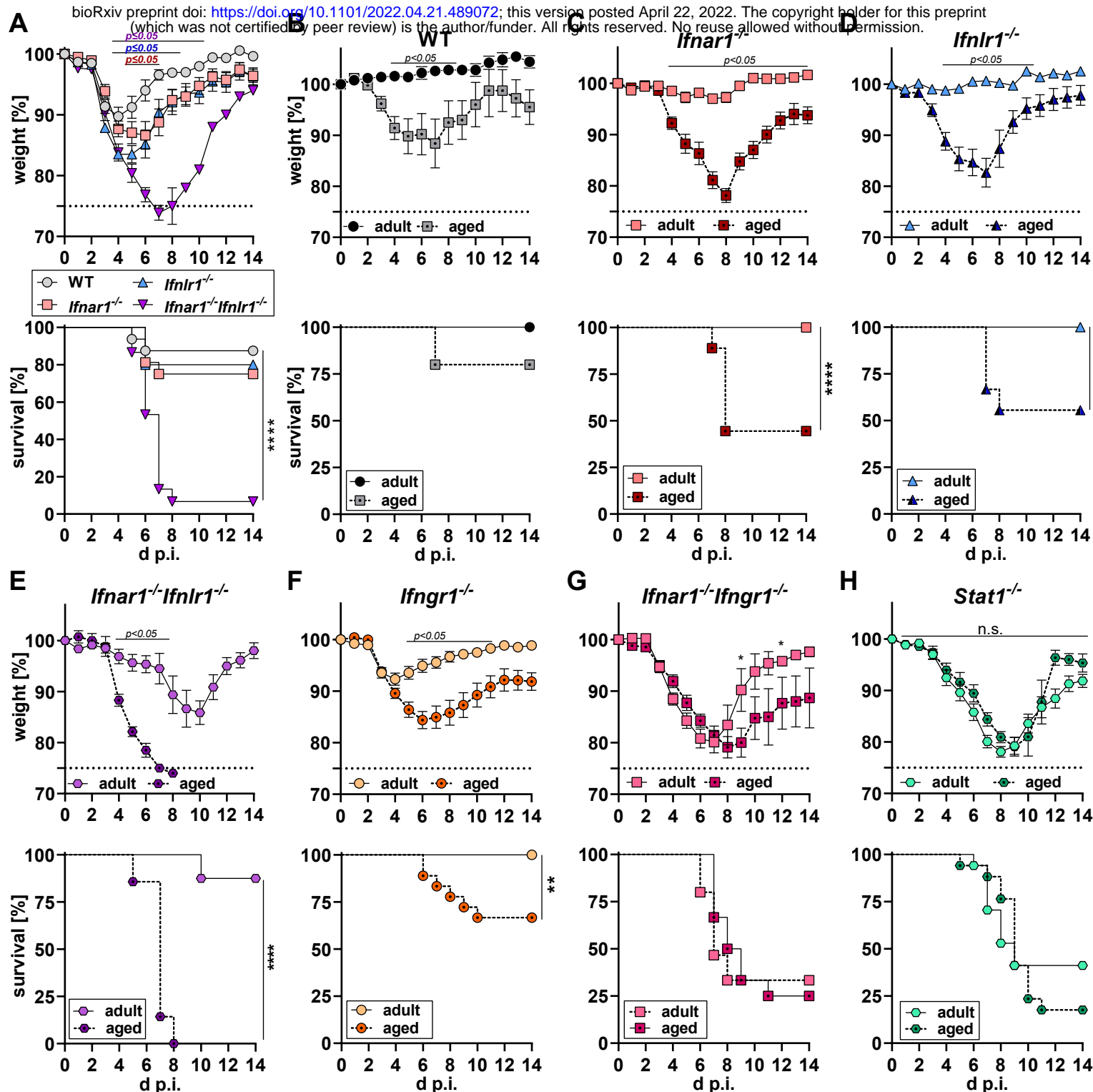
Figure 3 | SARS-CoV-2 MA20 efficiently replicates in upper airways and lungs of adult C57BL/6 mice inducing innate immune responses and tissue damage.

Figure 4 | Enhanced susceptibility of aged mice to SARS-CoV-2-induced disease correlates with increased viral load.
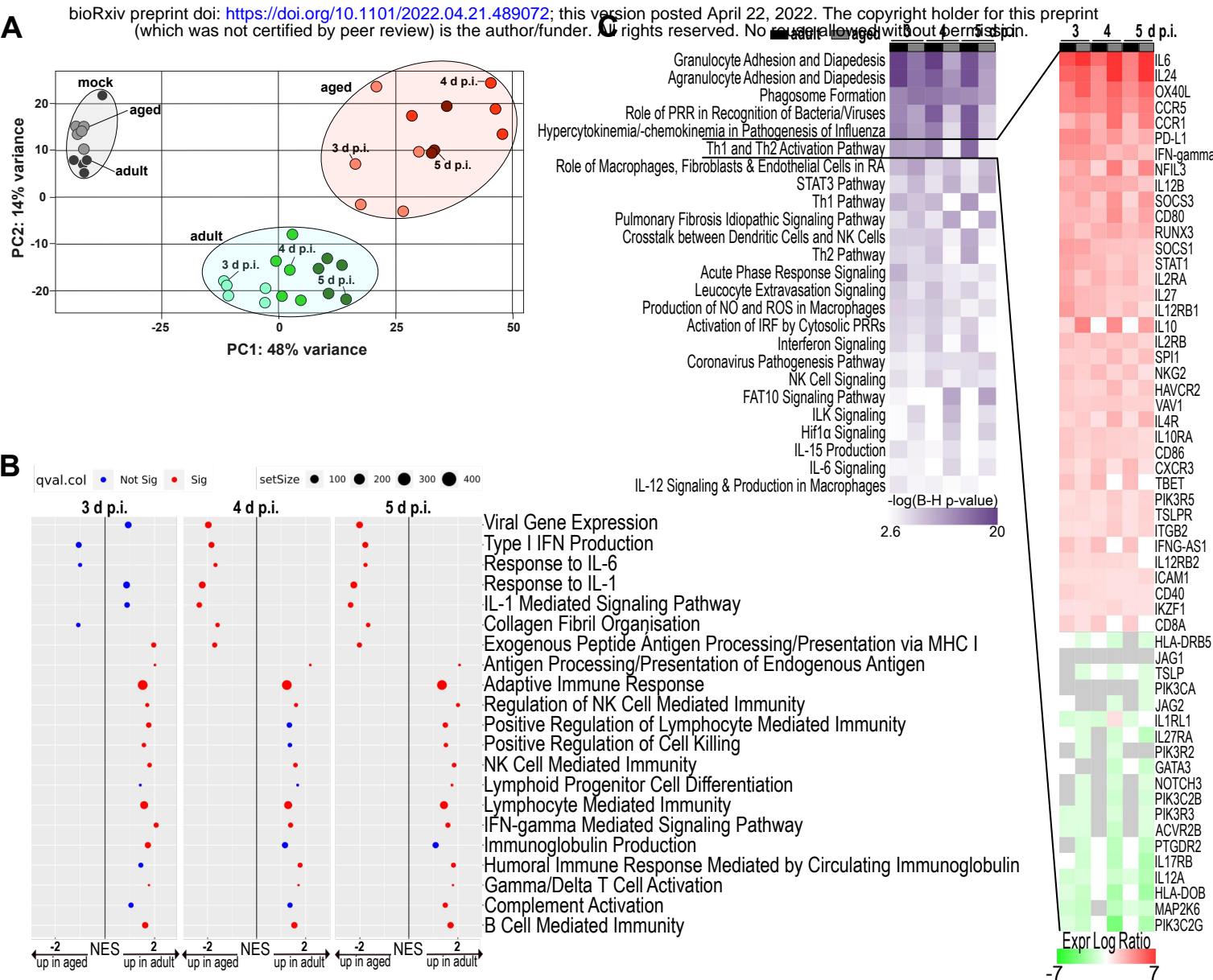
**Figure 5 | Immune response in SARS-CoV-2 infected aged mice is delayed, diminished and dysregulated.**

Figure 6 | Combined deficiency in type I and type II IFN signaling phenocopies age-dependent disease susceptibility.
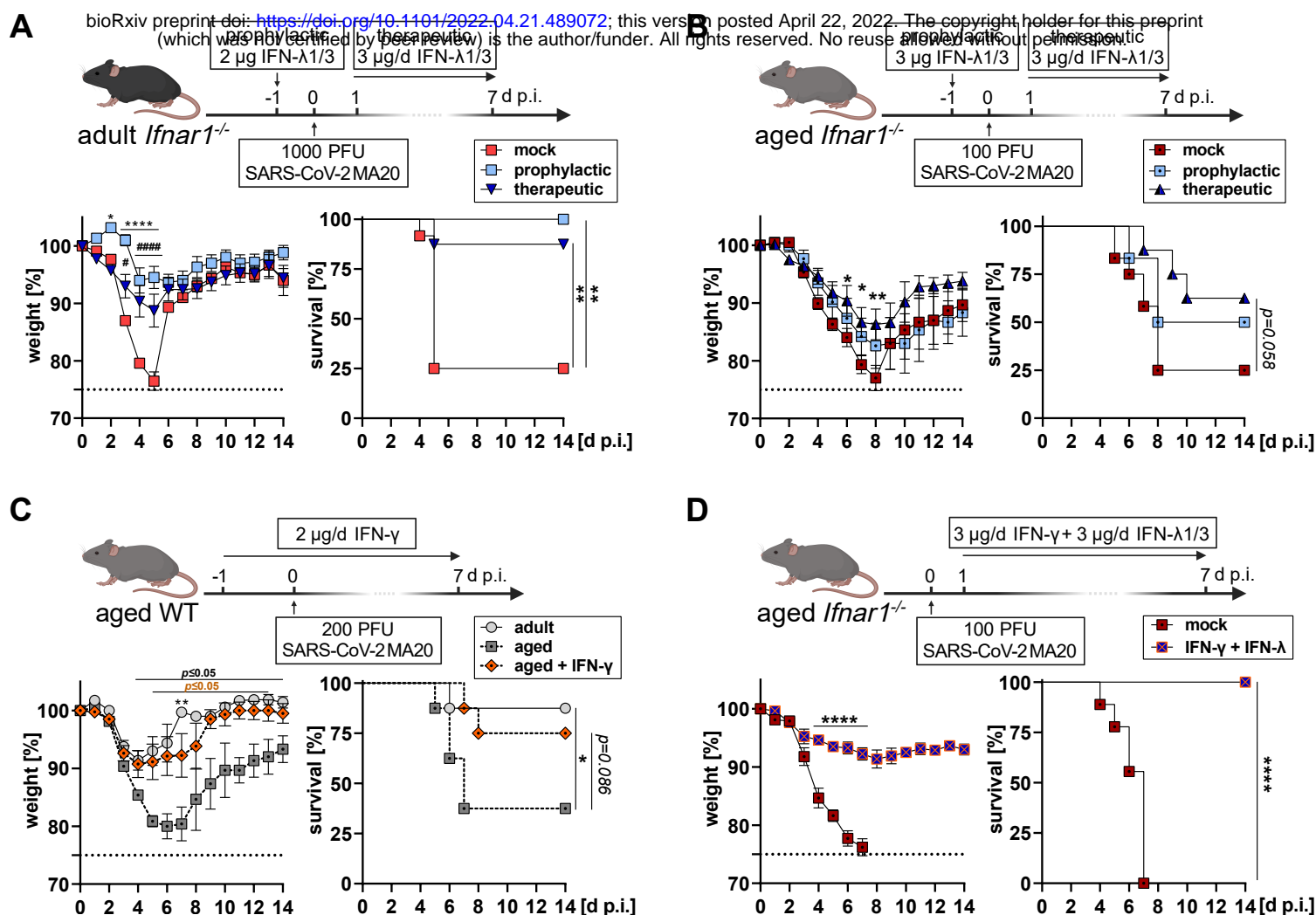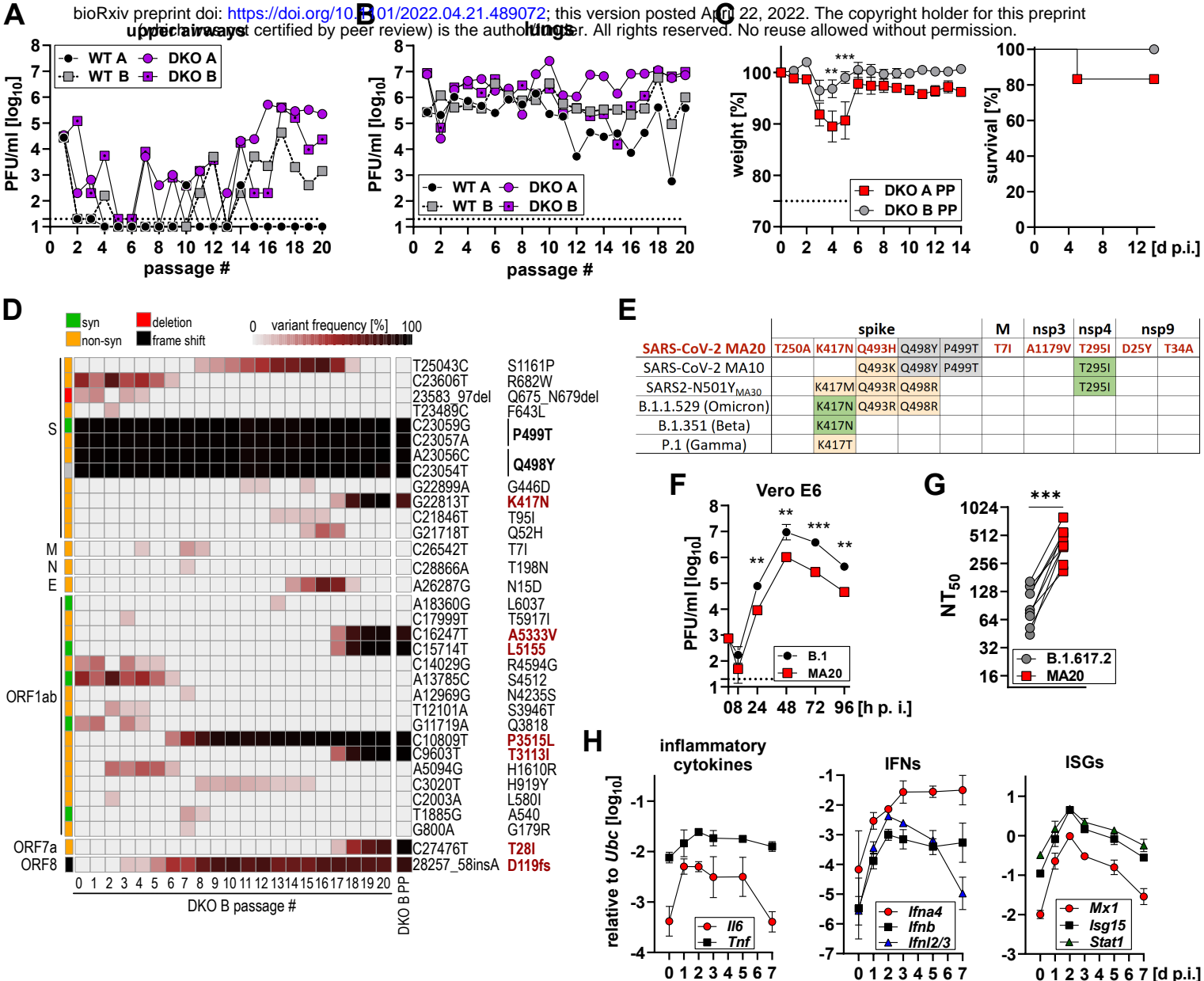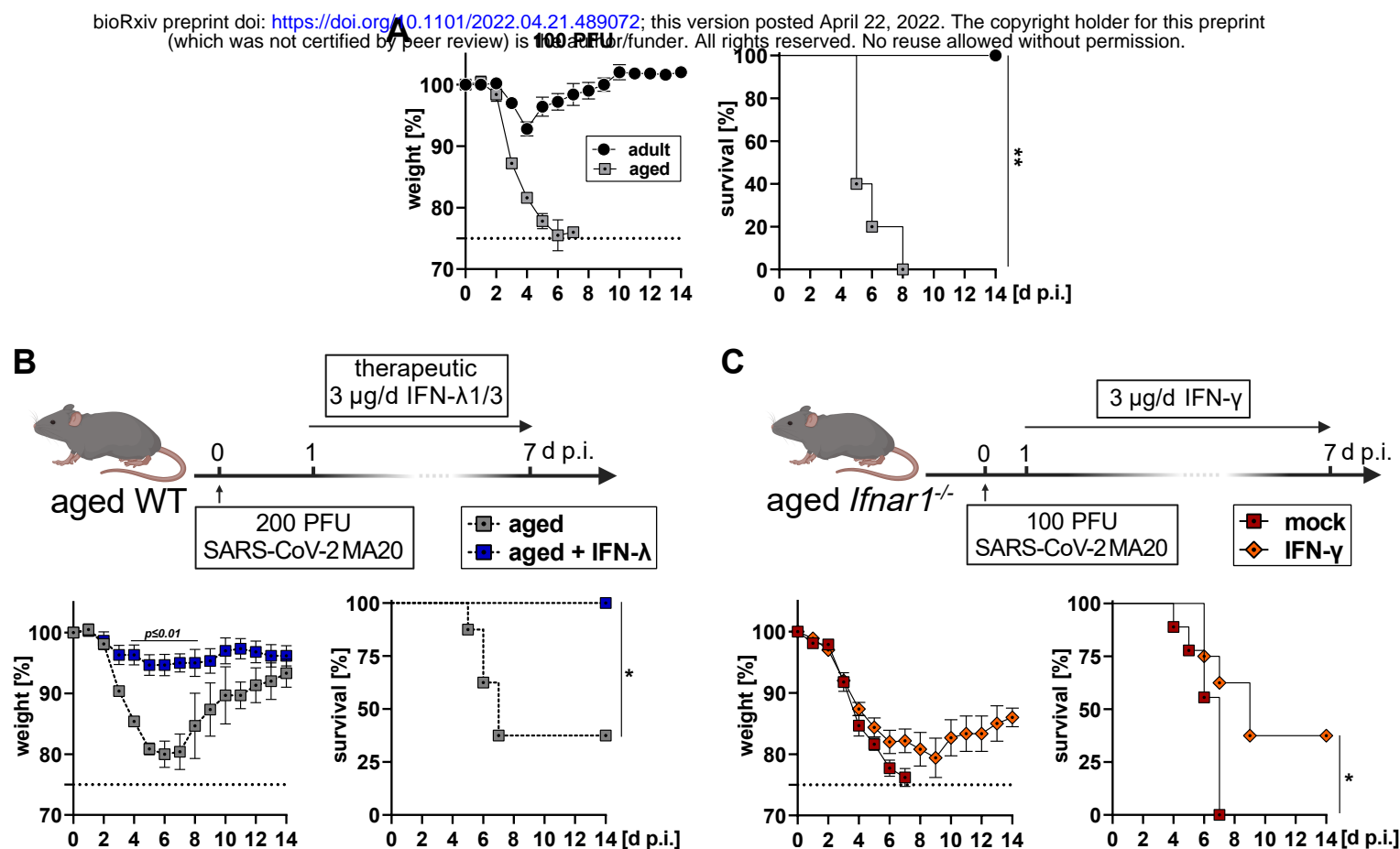
Figure 7 | Therapeutic administration of IFN-λ prevents SARS-CoV-2-induced lethality in absence of type I IFN immunity and supplementation of IFN-γ reverses age-dependent disease phenotype
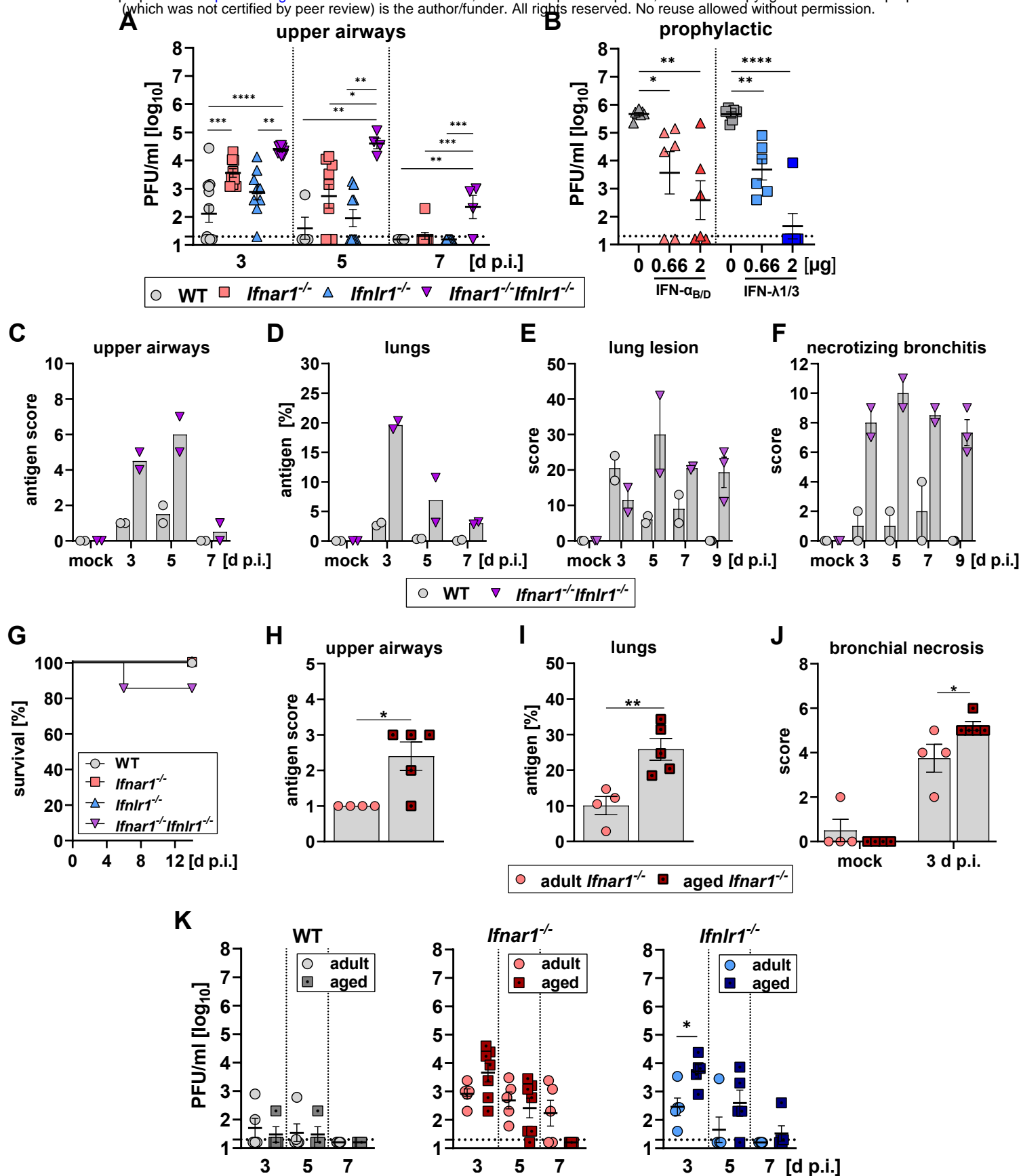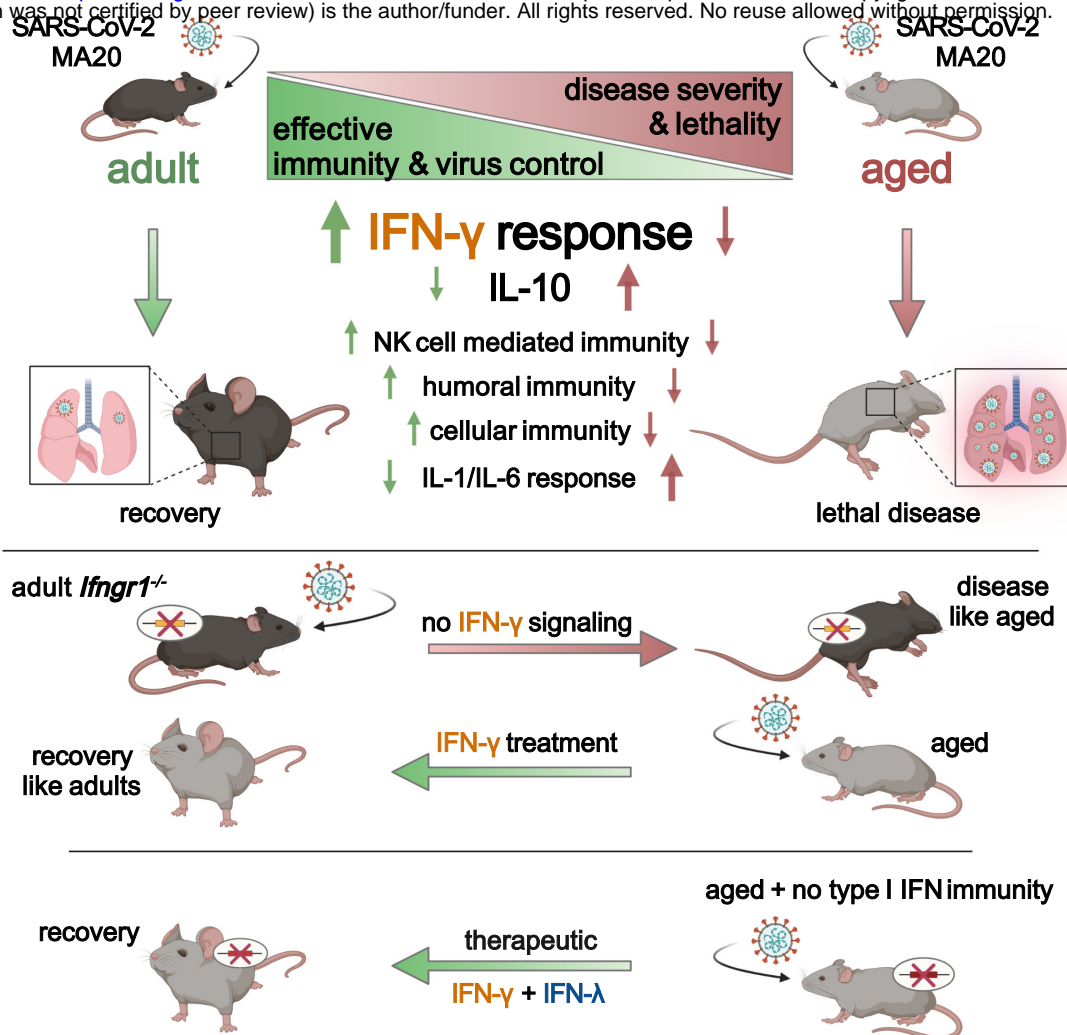
Figure S1 | Increased and prolonged replication of SARS-CoV-2 MA in mice lacking type I and/or type III IFN receptors.

Figure S2 | Serial passaging of MA SARS-CoV-2 in IFN receptor-deficient C57BL/6 mice allows for rapid host adaptation.

Figure S3 | Therapeutic administration of IFN-λ or IFN-γ reduces SARS-CoV-2 induced lethality in aged mice.

Figure S4 | Impaired immune response drives age-dependent virulence of SARS-CoV-2